

Implicit large eddy simulations of global solar convection: effects of numerical resolution in non-rotating and rotating cases

G. GUERRERO ^{1,2}, A. M. STEJKO ², A. G. KOSOVICHEV ², P. K. SMOLARKIEWICZ ³, AND A. STRUGAREK ⁴

¹*Physics Department, Universidade Federal de Minas Gerais
Av. Antonio Carlos, 6627, Belo Horizonte, MG 31270-901, Brazil*

²*New Jersey Institute of technology, Newark, NJ 07103, USA*

³*National Center for Atmospheric Research, Boulder, Colorado, USA*

⁴*AIM, CEA, CNRS, Université Paris-Saclay, Université Paris Diderot, Sorbonne Paris Cité, France*

Submitted to ApJ

ABSTRACT

Simulating deep solar convection and its coupled mean-field motions is a formidable challenge where few observational results constrain models that suffer from the non-physical influence of the grid resolution. We present hydrodynamic global Implicit Large-Eddy simulations (ILES) of deep solar convection performed with the EULAG-MHD code, and explore the effects of grid resolution on the properties of rotating and non-rotating convection. The results, based on low-order moments and turbulent spectra reveal that convergence could be achieved in non-rotating simulations provided sufficient resolution in the radial direction. The flow is highly anisotropic, with the energy contained in horizontal divergent motions exceeding by more than three orders of magnitude their radial counterpart. By contrast, in rotating simulations the largest energy is in the toroidal part of the horizontal motions. As the grid resolution increases, the turbulent correlations change in such a way that a solar-like differential rotation, obtained in the simulation with the coarser grid, transitions to the anti-solar differential rotation. The reason for this change is the contribution of the effective viscosity to the balance of the forces driving large-scale flows. As the effective viscosity decreases, the angular momentum balance improves, yet the force balance in the meridional direction lessens, favoring a strong meridional flow that advects angular momentum towards the poles. The results suggest that obtaining the correct distribution of angular momentum may not be a mere issue of numerical resolution. Accounting for additional physics, such as magnetism or the near-surface shear layer, may be necessary in simulating the solar interior.

Keywords: Solar interior (1500) — Solar differential rotation (1996) — Solar meridional circulation(1874) — Hydrodynamical simulations (767)

1. INTRODUCTION

Turbulent convection is observed at the solar photosphere in the form of granulation, with scales of several thousands of kilometers, and supergranulation, with scales of ~ 30000 km. From theoretical considerations it is expected that larger, self-similar, motions exist at deeper layers. Their characteristics, however, remain evasive to observations. The properties of solar convec-

tion at deeper layers are relevant for understanding the physical processes that drive and shape the large-scale flows observed in the Sun, namely the differential rotation (DR) and the meridional circulation (MC). Furthermore, they may be instrumental for the solar dynamo process.

The knowledge that we have about the deep turbulent motions is based on the one-dimensional mixing-length theory (MLT Böhm-Vitense 1958; Kippenhahn et al. 2013). The results of MLT models predict that spatial and temporal scales progressively increase with depth. Nevertheless, observations of turbulent motions

just beneath the supergranulation layer offered conflicting results such that the MLT scenario cannot be confirmed. From one side, [Hanasoge et al. \(2012\)](#) found that the larger scales have convective power several orders of magnitude smaller than the MLT prediction. On the other hand, the results of [Greer et al. \(2015\)](#) suggested spectral energies more in line with the theory, yet perhaps with larger power than expected. This ambiguity has often been called the solar convective conundrum.

[Proxauf \(2020\)](#) and collaborators have recently identified several incompatibilities in the comparison of the previous results, proposed the required corrections, and performed new inferences. Despite modifications, the disparity between the two helioseismic inferences still spans three to four orders of magnitude. Their new surface granulation tracking, and ring-diagram analysis measurements indicate that at low angular harmonic degree, ℓ , the trend of the power spectra agrees with the corrected results of [Hanasoge et al. \(2012\)](#), with slightly higher power (about one order of magnitude). Other analysis seem to confirm the existence of structures larger than supergranulation but with rather small power ([Hathaway & Upton 2021](#); [Getling & Kosovichev 2022](#)). At deeper layers, the properties of convection are still a mystery, and we rely on global simulations of turbulent rotating convection to get access at least to some of its characteristics. Unfortunately, simulations of solar convection are not exempt from difficulties.

The big goal of global convection simulations, precluding so far the possible development of magnetic fields, is developing motions able to carry out most of the solar luminosity, L_{\odot} , simultaneously producing a mean angular velocity in agreement with the helioseismic observations ([Schou et al. 1998](#)), and a meridional circulation with poleward migration at surface levels (e.g., [Ulrich 2010](#); [Hathaway & Upton 2014](#)). The meridional circulation profile in the deep convection zone is still under investigation and a matter of debate (see [Chen & Zhao 2017](#); [Gizon et al. 2020](#); [Stejko et al. 2021](#), for inferences with two and one meridional cells per hemisphere).

The parameter regime of the solar interior where convection must transport energy and angular momentum is characterized by the Rayleigh (Ra) number $\mathcal{O}(10^{20})$, the Reynolds number (Re) $\mathcal{O}(10^{12})$, and the Prandtl (Pr) number $\mathcal{O}(10^{-7})$ (see Table 2 in [Ossendrijver 2003](#)). The separation of the dynamical scales determined by these parameters requires an enormous resources to be resolved by direct numerical simulations (DNS). Modern supercomputers are still far from allowing DNS at such resolution. Thus, for the current DNS, the dissipative coefficients that define the non-dimensional numbers are orders of magnitude larger than the microscopic values

of viscosity and/or thermal conductivity. Considering that the values of these coefficients are consistent with the estimated turbulent dissipation, these simulations can be viewed as large-eddy simulations (LES) which preclude non-dissipative contribution of the unresolved scales.

In state-of-the-art simulations in which the radiative flux driving convection at the bottom of the convection zone corresponds to $L_{\odot} = 3.83 \times 10^{26}$ W, and the rotation imposed on the frame is the solar sidereal rotation, $\Omega_{\odot} = 2.97 \times 10^6$ s $^{-1}$, the convective heat flux results in enhanced turbulent velocities whose energy spectrum disagrees with the helioseismic observations described above ([Gizon & Birch 2012](#)). Additionally, higher velocities imply shorter convective correlation times, τ_c , and, therefore, larger Rossby numbers, which is the ratio between rotation and convection timescales, $Ro = P_{rot}/\tau_c$. This ratio is an indication of how much the motions are constrained by the Coriolis force. It is a fairly robust result of global convective simulations ([Käpylä et al. 2011](#); [Guerrero et al. 2013](#); [Gastine et al. 2014](#); [Featherstone & Miesch 2015](#)) that as the motions get less rotationally constrained (high Ro), the differential rotation profile results in faster poles and slow equator, at odds with the solar-like profile.

A solar-like differential rotation profile with an accelerated equator may be recovered by increasing the rotation rate by a factor of two or three ([Brown et al. 2008](#); [Hotta 2018](#)). Another alternative is diminishing the convective transport by increasing the radiative diffusion coefficient ([Miesch et al. 2008](#); [Käpylä et al. 2014](#); [Featherstone & Miesch 2015](#)), or by decreasing the luminosity of the simulation ([Guerrero et al. 2013](#); [Hotta et al. 2015](#)). The latter options artificially decrease the strength of the convective flows. In general, these alternatives decrease the Rossby number.

Large-scale or small-scale magnetic fields may also help to reproduce the solar differential rotation. They contribute in two different ways: by modulating the convective heat transport ([Fan & Fang 2014](#); [Karak et al. 2015](#); [Guerrero et al. 2019](#)) which decreases the turbulent velocities (lower Ro), and through the direct transport of angular momentum via the large and small scale Maxwell stresses. The contribution of the large-scale magnetic field has been verified by lower resolution simulations, which allow for a long temporal evolution and, therefore, the excitation and sustainment of the large-scale dynamo. The contribution of the small-scale dynamo has been recently identified in the high-resolution simulations by [Hotta & Kusano \(2021\)](#). They suggested that the small-scale magnetic field diminishes the convective power and that a meridional flow, developed to

balance the Maxwell stresses, transports angular momentum towards the equator. However, these simulations have run only for short periods of time, such that the large-scale magnetic field did not develop. Thus, there is still no clarity on the distribution of small-scale magnetic fields in the presence of large-scale dynamo, and it is uncertain what is the role of both contributions on the angular momentum transport.

Most simulations described above suffer from the contribution of unrealistically large dissipative coefficients caused by the limited spatial resolution. Large viscous dissipation, for instance, is needed to guarantee numerical stability. It is combined with the numerical dissipation associated with the numerical schemes. Both contributions directly affect the transport of linear and angular momentum, whereas in the Sun, the microscopic viscosity is negligible. Therefore, it is desirable albeit challenging to achieve converged solutions independent on numerical resolution. In other words, it is appealing having a system where the dissipation coefficients are insignificant and the dynamics is governed by well-resolved turbulent motions subject to well-defined boundary conditions. However, as discussed above, it does not seem to be the case for the current models of deep solar convection. As a matter of fact, very few works have systematically explored the role of resolution on the properties of convection. The work of [Featherstone & Hindman \(2016a\)](#) is one exception, for non-rotating convection in the sphere, with remarkable results. They are able to achieve simulations where the amplitude of the kinetic energy becomes independent of the Ra values, yet the distribution of root mean square (RMS) velocities and kinetic turbulent spectra continue changing as Ra further increases.

Large-eddy-simulations including explicit or implicit ([Grinstein et al. 2007](#)) turbulent sub-grid scale (SGS) contribution may be a computationally less expensive alternative to DNS of solar (stellar) convection and dynamo. LES have been routinely and successfully used in engineering and meteorological problems. This approach has also been used for modeling local convection and small-scale dynamo ([Wray et al. 2015](#); [Rogachevskii et al. 2011](#); [Kitiashvili et al. 2015](#)). Nevertheless, it has not been broadly considered in the problem of global simulations of solar and stellar convection and dynamo. This is understandable since, unlike laboratory experiments, or weather and climate studies, there is not sufficient available data nor convergent DNS results of the same problem. This prevents the comparison and characterization of the LES results and the SGS models.

The implicit LES simulations performed with the EULAG-MHD code, based in a non-oscillatory forward-

in-time algorithm, have been successful in reproducing at lower resolution some characteristics of the solar activity cycle ([Ghizaru et al. 2010](#)), and have also been used to study stellar activity ([Strugarek et al. 2017](#); [Guerrero et al. 2019](#)). In the code, the dynamical equations may be solved in their inviscid form, with the viscous contribution given by the minimized truncation terms, allowing to achieve the higher possible level of turbulence, i.e., a larger value of Re, for any resolution. In this form, it is less computationally expensive to search for solutions to the problem independent of the non-physical influence of numerical resolution. We have demonstrated convergence in the solutions of simulations of 2D convection for a range of different mesh sizes [Nogueira et al. \(2022\)](#). The low-order moments in the physical space as well as the turbulent spectra of kinetic and thermal energy were used as criteria of convergence. We attribute the convergence of the results in the low-resolution cases to the implicit SGS viscosity of the non-oscillatory discrete advection method, which allows the back-scatter of energy from small to large scales and dissipation at the minimal scale, close to the limit of numerical resolution. For progressively larger resolutions, however, large and small scale motions coexist in a system dominated by a mesh-independent turbulent dissipation. In these cases the contribution from the small scales seems to be resolved.

In this paper, we continue the study presented in [Nogueira et al. \(2022\)](#) while approximating our numerical model to the solar interior by considering spherical geometry. Additionally, we consider the effects of rotation on the turbulent motions and explore the development of mean flows in models where all parameters are kept constant except the grid resolution. This problem is more complicated than the Cartesian case. On the one hand, the spherical geometry imposes curvature effects and numerical stiffness in polar regions. On the other hand, gravity and rotation result in strongly anisotropic convective motions upon which the amount of viscous resistance, wherever is its origin, turns out to be highly relevant. We anticipate that for non-rotating cases, hints of convergence are achieved at a resolution consistent with the Cartesian cases. For the rotating cases, the resulting large-scale motions are substantially dependent on the resolution due to the decreasing contribution of effective viscosity to the net transport of angular momentum. We characterize these changes through a comparative analysis of the spectral properties of the fluid, and the balance of the azimuthal and meridional forces that drive these large-scale motions. To differentiate the most robust features of global convection from those that seem to be model dependent, we extend our

comparison to previous findings of similar models, and to solar observations, when possible. Even though we do not achieve convergence, the analysis contributes to understanding the sustainment of solar mean-flows and allows us to hypothesize possible ways to achieve solutions to the convective conundrum.

This paper is organized as follows. In Sect. 2, we describe the numerical model. The results of non-rotating and rotating cases are presented in Sect. 3, and in Sect. 4, we discuss our findings and expose the conclusions of this work.

2. NUMERICAL MODEL

The EULAG-MHD code (Smolarkiewicz & Charbonneau 2013) — a specialized variant of the original EULAG code (Prusa et al. 2008) — is used to perform global anelastic convection simulations. EULAG-MHD is based on the multidimensional positive-definite advection transport algorithm (MPDATA; Smolarkiewicz 2006). It is a non-oscillatory forward-in-time advection solver with second-order accuracy in space and time. The code allows simulations to be run as ILES without explicit dissipation, yet it also may be used for DNS with explicit dissipation. The domain corresponds to a global spherical shell with the radial coordinate, r , covering the upper fraction of the radiative zone, from $r_b = 0.6R_\odot$, and the convection zone (CZ) up to $r_t = 0.96R_\odot$. We exclude the upper layers of the CZ where compressibility and radiative transfer play a major role in the dynamics of convection.

The code integrates the following set of Navier-Stokes equations governing mass, momentum, and energy conservation,

$$\nabla \cdot \rho_r \mathbf{u} = 0, \quad (1)$$

$$\frac{d\mathbf{u}}{dt} + 2\boldsymbol{\Omega} \times \mathbf{u} = -\nabla\pi' - \mathbf{g}\frac{\Theta'}{\Theta_r}, \quad (2)$$

$$\frac{d\Theta'}{dt} = -\mathbf{u} \cdot \nabla\Theta_a - \alpha\Theta' \quad (3)$$

where $d/dt = \partial/\partial t + \mathbf{u} \cdot \nabla$, \mathbf{u} is the velocity field in a frame rotating with angular velocity $\boldsymbol{\Omega} = (\Omega_r, \Omega_\theta, \Omega_\phi) = \Omega_0(\cos\theta, -\sin\theta, 0)$, ρ_r is the reference state density, which in the anelastic approximation is a function of radius only (Lipps & Hemler 1982); π' is the density normalized pressure perturbation, p'/ρ_r ; $\mathbf{g} = -g\hat{\mathbf{e}}_r$ is the gravity acceleration adjusted to fit the solar gravity profile, and Θ is the potential temperature defined as $\Theta = T(P_b/P)^{R/c_p}$, where T is the temperature, P is the pressure, P_b is the pressure at the bottom of the domain, $R = 13732 \text{ J K}^{-1} \text{ kg}^{-1}$ is the universal gas constant for a monoatomic hydrogen gas, and $c_p = 2.5R$, is the specific heat at constant pressure. The potential temperature is

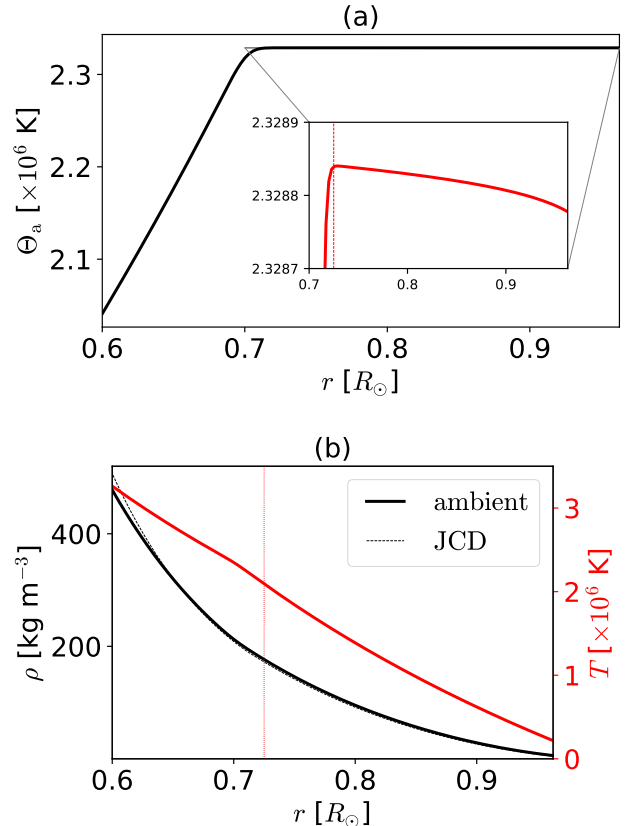


Figure 1. (a) Radial profile of the ambient potential temperature, Θ_a . The insert shows a close-up for $0.7 < r/R_\odot < 0.96$ depicting a negative radial gradient of Θ_a . The difference between the bottom and top of the unstable layer is 62 K. (b) Radial profiles of the ambient density (black line) and temperature (red line). The dotted lines correspond to the solar structure model of Christensen-Dalsgaard et al. (1996). From the bottom to the top of the domain there are ~ 4.5 density scale heights. From the base of the convection zone, $r > 0.7R_\odot$ there are ~ 3.7 density scale heights. The vertical red lines show the bottom of the unstable layer located at $r = 0.725R_\odot$.

equivalent to the specific entropy through the relation $ds = c_p d(\ln\Theta)$. The subscripts r and a refer to the reference and ambient states, and the superscript $'$ means perturbations of a quantity about the ambient profile. Perturbations of Θ are related to perturbations of temperature by the anelastic approximation, $T' = \Theta' T_a / \Theta_a$. The energy equation contains a term forcing the adiabatic perturbations about the ambient state and a thermal relaxation term that damps these perturbations in an inverse time scale, $\alpha = 1/\tau$ (cf. Cossette et al. 2017, for a discussion).

The ambient state defining the thermodynamic variables, ρ_a , Θ_a , and T_a in equations (1) - (3) is a par-

ticular solution of the hydrodynamics equations. In this work, the ambient state considering hydrostatic equilibrium for a non-rotating atmosphere is constructed by solving the following equations,

$$\frac{\partial T_a}{\partial r} = -\frac{g}{R(m+1)}, \quad (4)$$

$$\frac{\partial \rho_a}{\partial r} = -\frac{\rho}{T_a} \left(\frac{g}{R} + \frac{\partial T_a}{\partial r} \right), \quad (5)$$

where $m = m(r)$ is the polytropic index. Solutions of equations (4) and (5) with $m \geq 1.5$ correspond to stable stratification, while solutions for $m < 1.5$ correspond to convectively unstable states.

The ambient state with a stable layer at the bottom of the domain is built by setting $m_s = 2.5$ for $r \leq 0.7R_\odot$, and a marginally unstable convection zone with $m_u = 1.49997$ for $r > 0.7R_\odot$. This is achieved by considering a radial profile of the polytropic index,

$$m(r) = m_s - \frac{1}{2}(m_s - m_u) \left[1 + \operatorname{erf} \left(\frac{r - r_1}{w} \right) \right], \quad (6)$$

where the transition between zones of different m is made through the erf functions with $r_1 = 0.7R_\odot$ and $w = 0.01R_\odot$. Equations (4) and (5) are integrated numerically with $\rho_{r_1} = 208 \text{ kg/m}^3$ and $T_{r_1} = 2.322 \times 10^6 \text{ K}$ at the interface between the stable and the unstable layers. The pressure is computed via the ideal gas equation of state, $P_a = R\rho_a T_a$. The resulting profile of Θ_a as a function of radius is shown in Figure 1(a). In the convective zone, the slope of Θ_a is slightly negative with respect to the r coordinate as it can be seen in the figure insert. The negative slope of Θ_a ensures that this zone is unstable to convection, with the difference of Θ_a between the bottom and top of the convectively unstable layer being 62 K. The reference potential temperature $\Theta_r = T_{r_1}$. Finally, for all the simulations, $\alpha = 1/\tau = 1.29 \times 10^{-8} \text{ s}^{-1}$ is considered. Fig. 1(b) shows the radial profiles of the density, ρ_a , and the temperature, T_a . The entire radial domain encompasses 4.5 density scale heights with 3.7 density scale heights corresponding to the unstable layer.

The boundary conditions for this setup are: impermeable, stress-free conditions for the velocity field at the two radial ends of the domain. Null convective radial flux is considered as thermal boundaries at the bottom and top, as it has been used in previous works in the literature (e.g., Fan et al. 2003; Hotta et al. 2015). For most of the cases the initial conditions are white noise perturbations in Θ' , introduced only in the unstable layer and with maximum amplitude 0.1 K.

3. RESULTS

In the simulations discussed below, the ambient stratification and the thermal relaxation time scale are kept constant, therefore, the forcing and the thermal relaxation terms in Eq. (3) are theoretically the same in all models (i.e., in the hypothetical limit of the converged numerical solutions). Non-rotating models ($\Omega_0 = 0$) with five different numerical resolutions (see Table 1) are presented. Based on the results of these models three rotating simulations, with $\Omega_0 = 3.03 \times 10^{-6} \text{ s}^{-1}$ ($P_{\text{rot}} = 24$ days) for three different resolutions are performed. For this rotation rate, the low-resolution case produces a solar-like differential rotation profile. The runtime of each simulations, here considered as the physical time, in years, that the variables are evolved, is presented in Table 1. The simulation R8 is started from a remeshed snapshot of the simulation R4 in the relaxed state and ran for ~ 2.8 Earth years. The temporal averages are calculated from outputs with a cadence of 1 month over a time range of 5 years. For simulation R8 only 6 months of simulated data were considered.

3.1. Non-rotating convection

We first explore the effects of numerical resolution in the low-order moments and the spectral properties of non-rotating simulations. Figure 2 shows snapshots of the radial, latitudinal, and longitudinal velocities, w , v , and u , for simulations R1-R8 (from top to bottom). The graphs show the level of detail reached by different resolutions. The amplitude of the velocity components increases as evidenced by brighter colors from the top to the bottom panels. It is also evident that in models R1 and R2 the grid size in regions with small density scale height, i.e., close to the model's top, is insufficient to resolve the scales of the sub-surface motions. This is observed in the RMS profiles of the radial and longitudinal components of the velocity field, $w_{\text{rms}} = \sqrt{\langle w^2 \rangle_{\phi\theta}}$ and $u_{\text{rms}} = \sqrt{\langle u^2 \rangle_{\phi\theta}}$, as well as in the total RMS velocity, $U_{\text{rms}} = \sqrt{\langle u^2 + v^2 + w^2 \rangle_{\phi\theta}}$. Throughout the paper, angular brackets $\langle \rangle_{\phi\theta}$ correspond to averages over the horizontal directions and time, $\langle \rangle$ to volume and time averages over the convective shell, and overline corresponds to average over longitude and time. In w_{rms} the lack of resolution appears as flat profile for $r > 0.9R_\odot$ for simulation R1 and for $r > 0.93R_\odot$ for R2, see Fig. 3(a). In u_{rms} and U_{rms} , it appears as a local minimum that may be observed in the profiles of the same simulations close to the upper boundary, Fig. 3(b and c). This undesirable property was reported in the 2D Cartesian cases (Nogueira et al. 2022). The black dashed line presented in the figure corresponds to simulation R1x, it has the same horizontal resolution as

Table 1. Simulation parameters and results

Simulation	N_ϕ, N_θ, N_r	dt [s]	Runtime [years]	$\langle U_{\text{rms}} \rangle$ [m/s]	$\langle \Theta' \rangle$ [K]	$\langle L_e \rangle$ [L_\odot]	Ro
R1	128,64,64	1400	200	54.07	21.49	0.38	-
R2	256,128,128	500	80	51.70	13.78	0.25	-
R4	512,256,256	200	26	61.92	9.45	0.17	-
R8	1024,512,512	50	2.8	69.24	9.23	0.14	-
R1x	128,64,256	800	40	65.15	9.37	0.16	-
R1x24	128,64,256	800	80	45.85	9.50	1.30	0.56
R2x24	256,128,256	600	60	46.90	9.60	1.37	0.58
R4x24	512,256,256	200	20	52.32	9.54	1.34	0.65

NOTE—Parameters and results of the simulations presented in this work. The angular brackets, $\langle \rangle$, correspond to volume and temporal averages considering only the convection zone, i.e., an average over radius of the profiles presented in Figs. 3, 4, 8, and 9. The Rossby number is defined as, $\text{Ro} = P_{\text{rot}}/\tau_c$, where, $\tau_c = \ell_c/\langle U \rangle_{\text{rms}}$, is the convective turnover time. For simplicity, the convective correlation length, ℓ_c , is defined as the thickness of the unstable layer.

R1, but with a fourfold resolution in the radial direction ($N_\phi = 128, N_\theta = 64, N_r = 256$). While there are small departures from the cases with higher resolution, especially in the radial velocity, it is remarkable the similarity between case R1x and high resolution cases R4 and R8.

The spherical simulations show radial motions which have a maximum roughly at the center of the convection zone ($r \sim 0.85R_\odot$). The amplitude of w_{rms} slightly increases from the low to the high resolution cases, with a rather small difference between case R4 and R8. The longitudinal velocity, u_{rms} , shows larger amplitudes at the bottom of the convection zone resulting from the encounter of fast downward plumes with the rigid stable layer. As a consequence, the profiles of u_{rms} as a function of radius have a minimum in the bulk of the convection zone at about $0.8R_\odot$. This feature does not appear in simulations that consider only the convection zone, where a stress-free boundary condition is imposed at their base (e.g., Fan & Fang 2014; Hotta 2018). It is important because it creates a steeper transition between convective and radiative layers.

The averaged values of the perturbations of potential temperature are presented in Fig. 3(d). Despite simulations R1 and R2, which show higher values of Θ' at the upper levels, the profiles for models R1x, R4 and R8 are rather similar. The profile of the luminosity, $L_e = 4\pi r^2 F_e$, carried by the enthalpy flux, $F_e = R_g c_p \rho \langle w \Theta' \rangle_{\phi\theta}$, for all non-rotating cases, is shown with solid lines in Fig. 4(a). The profiles are normalized to the solar luminosity, L_\odot . Notice that L_e decreases with the increase of resolution, and has a similar profile for simulations R1x and R4. The higher values reached

in the low resolution simulations reflect the strong perturbations of Θ in the upper layers of the domain in Fig. 3(d). The profile for case R8 is different perhaps due to insufficient statistics. The inset of the Fig. 4(a) shows the bottom of the convection zone where the enthalpy flux is negative. This thin layer, where the correlations between w (mostly negative due to fast downward plumes) and Θ' (positive) are negative, is associated with overshooting. It is roughly zero for case R1 and increases with the grid size until reaching roughly similar values for the higher resolution simulations R4 and R8. The luminosity carried by the kinetic energy flux, $L_k = 4\pi r^2 F_k$, with $F_k = \rho \langle w(u^2 + v^2 + w^2) \rangle_{\phi\theta}$ is presented in the same panel with dotted lines. The flux is negative for all cases with minimum values reached by the high resolution simulations.

3.1.1. Spectral analysis

In this section we present the spectral properties of the non-rotating simulations. We are interested in the distribution of energy among convective scales for the different components of the flow. The library SHTns (Schaeffer 2013)¹, is used to compute the spectral representation of the vector velocity field as,

$$\mathbf{u}(\theta, \phi) = \sum_{\ell} \sum_{m=-\ell}^{\ell} q_{\ell}^m \mathbf{Q}_{\ell}^m(\theta, \phi) + s_{\ell}^m \mathbf{S}_{\ell}^m(\theta, \phi) + t_{\ell}^m \mathbf{T}_{\ell}^m(\theta, \phi), \quad (7)$$

¹ See also <https://www2.atmos.umd.edu/~dkleist/docs/shtns/doc/html/index.html>

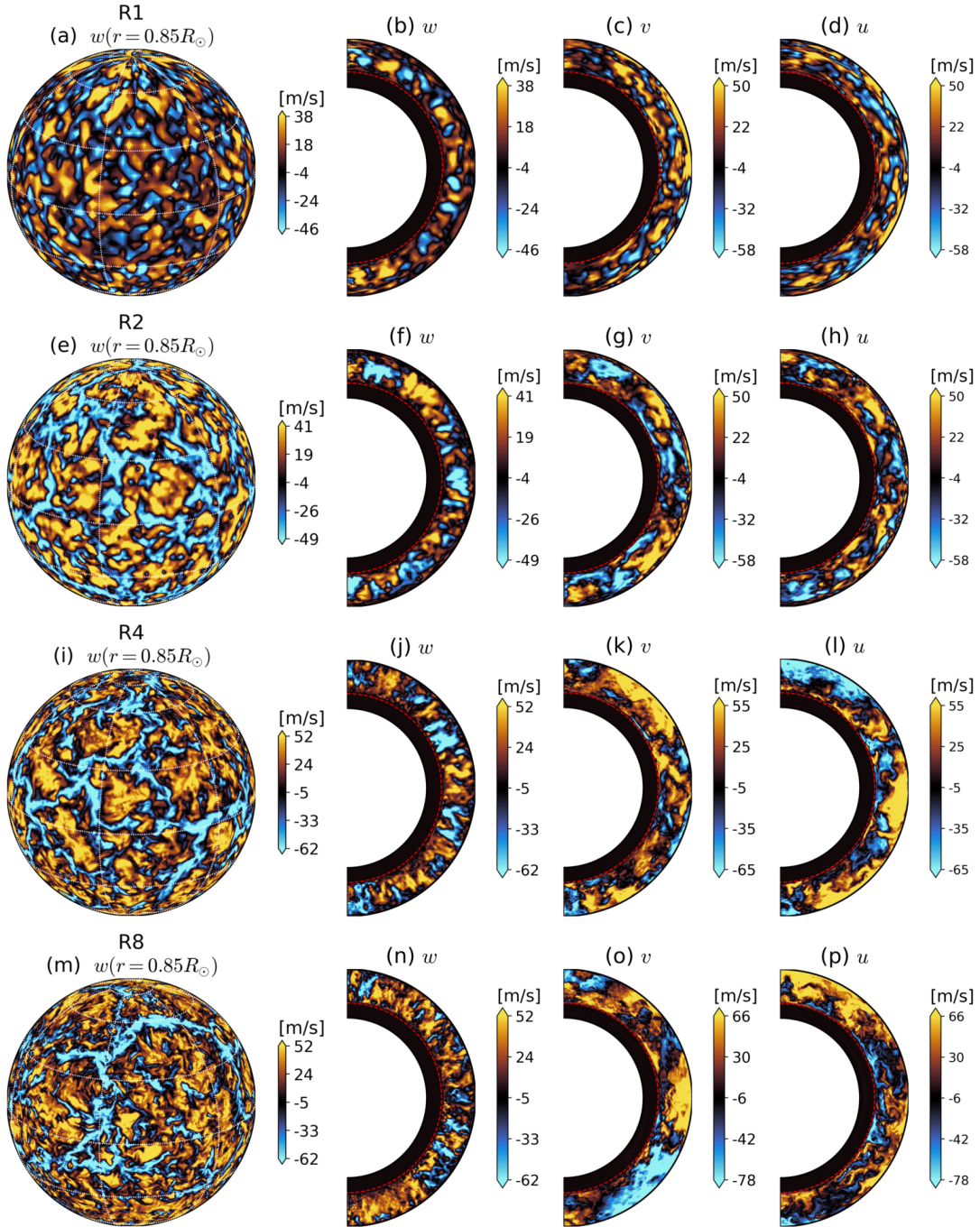


Figure 2. Instantaneous snapshots of the velocity components for simulations R1 to R8, from top to bottom. The radial velocity, w is presented in the orthographic projection (panels a, e, i, and m), and in the meridional plane (b, f, j, and n). The latitudinal, v (panels c, g, k, and o) and the longitudinal, u (panels d, h, l, and p) components are presented in the meridional plane. The thin dashed red line shows the transition between the stable and unstable layers.

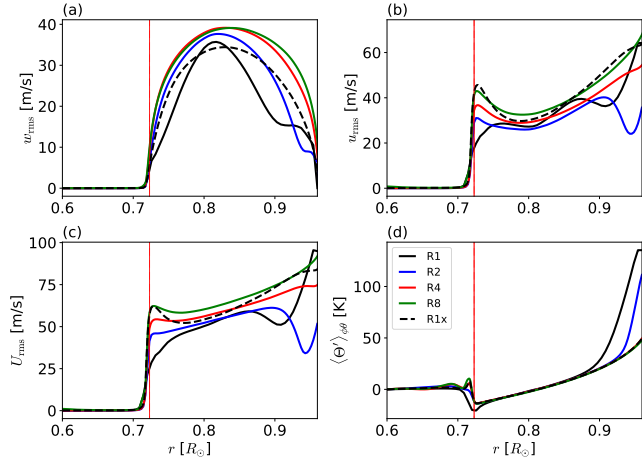


Figure 3. Radial profiles of w_{rms} (a), u_{rms} (b), the total U_{rms} (c); and the perturbations of potential temperature (d). The profile of the latitudinal component v_{rms} is similar to u_{rms} . The averaging was performed in the horizontal directions and time. The thin vertical lines show the bottom of the unstable layer.

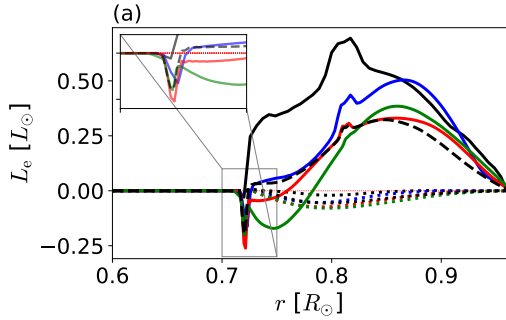


Figure 4. Luminosity carried by the enthalpy flux, $L_e = 4\pi r^2 R_g c_p \rho \langle w \Theta' \rangle_{\phi\theta}$ (solid lines), and the kinetic energy flux, $L_k = 4\pi r^2 \rho \langle w(u^2 + v^2 + w^2) \rangle_{\phi\theta}$ (dotted lines) for the non-rotating simulations presented in Table 1. The color coding of the lines is the same as in Fig. 3. The inset shows the overshooting region with negative values of L_e .

where,

$$\mathbf{Q}_\ell^m = Y_\ell^m \hat{\mathbf{e}}_r \quad (8)$$

$$\mathbf{S}_\ell^m = r \nabla Y_\ell^m \quad (9)$$

$$\mathbf{T}_\ell^m = -\mathbf{r} \times \nabla Y_\ell^m, \quad (10)$$

and Y_ℓ^m are spherical harmonics of degree ℓ and order m , with $-\ell \leq m \leq \ell$. The coefficients q_ℓ^m , s_ℓ^m and t_ℓ^m are the radial and transverse components of the velocity vector. Under this decomposition, the spherical harmonic representation of the total kinetic energy as a

function of the harmonic degree ℓ is given by

$$\tilde{E}(\ell) = \sum_{m=-\ell}^{\ell} |q_\ell^m|^2 + \ell(\ell+1) (|s_\ell^m|^2 + |t_\ell^m|^2). \quad (11)$$

The kinetic energy spectra for all non-rotating simulations (see legend in the figure) are presented in Fig. 5 for three different depths, (a) $r = 0.95 R_\odot$, (b) $r = 0.85 R_\odot$, and (c) $r = 0.75 R_\odot$. As it could have been anticipated from the results in physical space, as a consequence of poorly resolved motions the simulations R1 and R2 have less kinetic energy at the upper layers, and show an excess of energy at large wave numbers. However, simulations R4 and R8 have a similar spectra with maximum amplitude at $\ell \sim 3$. In the middle and bottom of the convection zone the energy at the largest scales, $\ell < 4$, increases with the resolution. This indicates that the effective viscosity is decreasing and its action shifting towards the smaller scales. For $\ell \gtrsim 4$, the kinetic spectra of simulations R2-R8 are similar. With the increase of the resolution the spectra extend over more scales, reaching about two decades of ℓ for R8.

As for the energy cascade from the most energetic scales towards the dissipative scales, the simulations show a scaling slower than the Kolmogorov law, $k^{-5/3}$ (Kolmogorov 1941), especially in the middle and bottom of the convection zone. This result is expected given the buoyant force in an atmosphere with significant density stratification. Qualitative inspection shows that the Kolmogorov rule seems to exist in small regions of the inertial scale.

A surprising aspect of the figure is the spectra from simulation R1x presented with black dashed lines. Although this case has a coarse horizontal resolution, equivalent to R1, and high resolution, equivalent to case R4, only in radius, its kinetic power spectra are compatible with the highest resolution cases. The comparison shows that simulation R1x has an excess of energy in the largest scales. However, the energies at the inertial range as well as the turbulent scaling have good agreement with R4 and R8.

To assess the relevance of the present results, we compare them with solar supergranulation motions, which are weakly influenced by rotation. Although their nature is still controversial, recent works point toward a buoyant convective origin (Cossette & Rast 2016; Rincon & Rieutord 2018). Recently, Rincon et al. (2017) developed analytical scaling laws for the spectral behavior of a flow in a stratified atmosphere in the presence of buoyancy, i.e., anisotropic turbulence. They successfully compared these laws with the spectra of supergranulation reconstructed from Doppler and photometric measurements of the HMI instrument on the SDO

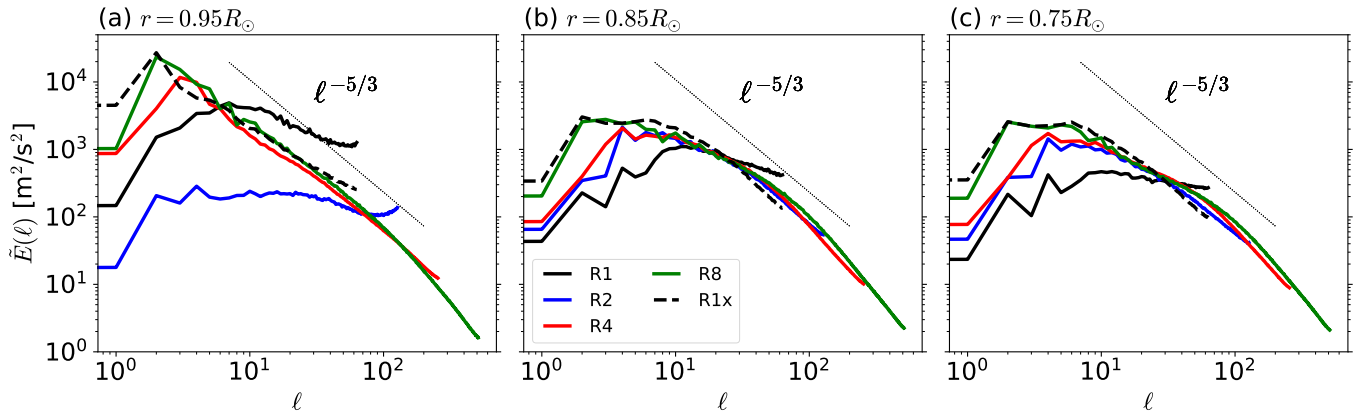


Figure 5. Turbulent kinetic power spectra for simulations with different resolutions R1-R8 (see color correspondence in the legend), at three different depths, from left to right. The black dashed line corresponds to a simulation with the same horizontal resolution than R1 but 256 grid points in the radial direction. The dotted line shows the $\ell^{-5/3}$ Kolmogorov scaling.

satellite (Scherrer et al. 2012), and decomposed in the spherical harmonic components. This supports the hypothesis that supergranulation is a particular scale of buoyantly driven convection. It is possible to evaluate whether the convectively driven motions developed in the simulations above compare with their results.

Fig. 6 shows the kinetic energy spectra decomposed into the radial (black lines), spheroidal (blue) and toroidal (yellow) components at $r = 0.95R_\odot$ for simulations R1 (panel a) to R8 (d), and R1x (presented in panel c). These components are obtained by separating the terms in the RHS of Eq. (11),

$$\begin{aligned} \tilde{E}_Q(\ell) &= \sum_{m=-\ell}^{\ell} |q_\ell^m|^2, \\ \tilde{E}_S(\ell) &= \sum_{m=-\ell}^{\ell} \ell(\ell+1) |s_\ell^m|^2, \\ \tilde{E}_T(\ell) &= \sum_{m=-\ell}^{\ell} \ell(\ell+1) |t_\ell^m|^2. \end{aligned} \quad (12)$$

Under this decomposition, \tilde{E}_S and \tilde{E}_T are measurements of the flow divergence and vorticity in the (ϕ, θ) plane, respectively. In this sense, toroidal does not correspond to the longitudinal component of the flow, as usually assumed in mean-field theory. In this representation, there is a striking difference of simulations R1 and R2 from all the others. These simulations have more energy in the toroidal motions than in the radial and spheroidal motions. The distribution of energy changes in simulation R2, but a convergent pattern seems to appear for the cases R4 and R8. The results clearly show anisotropic turbulence, with the spheroidal, divergent, part of the motions having $\sim 10^3$ times more energy than the radial flows. In panel (c), simulations R4 (continuous lines)

and R1x (dashed lines) are compared. Both cases show similar spectral properties. In panel (d) the red dotted lines correspond to the scaling laws for spheroidal and radial motions derived by Rincon et al. (2017). The black dotted lines correspond to their Kolmogorov equivalents. The scaling laws followed by the motions in our simulations R4, R8 and R1x, certainly of buoyant origin, compare well with those of Rincon et al. (2017). However, the Kolmogorov laws are also plausible, and it is hard to distinguish what law is followed and in what range of the spectra.

Caution is needed in this comparison because the simulations correspond to a thick shell and develop scales considerably larger than supergranulation (supergranulation has its maximum energy at $\ell \sim 120$, whereas the simulations results show peaks at $\ell \sim 3$). Nevertheless, the energy distribution among the different components of the velocity, the morphology of the spectral curves, with the spheroidal motion peaking at a large scale, the radial kinetic energy having a kink at the same scale but peaking at a smaller one, and the compatible turbulent scaling laws, demonstrate that simulations R1x, R4 and R8 capture well the properties of convective motions unconstrained by rotation.

It is also worth comparing the findings described above with those of other in similar simulations. The spherical high resolution simulation, case SD, presented in Hotta et al. (2019) has a radial profile of the RMS velocity that is qualitatively similar to the profiles of U_{rms} presented in Fig. 3(c). Because in their simulations convection carries almost the entire solar luminosity, the amplitude of the velocity is larger. The turbulent kinetic spectrum of this case has about two orders of magnitude more energy in the horizontal than in the radial motions (see also Hotta et al. 2014). In the cases presented here,

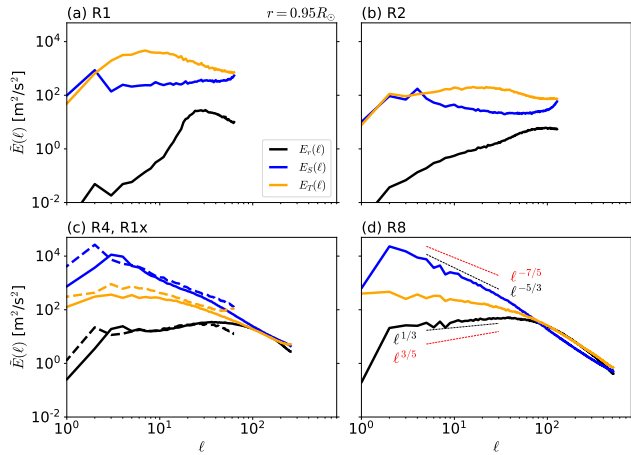


Figure 6. Kinetic power spectra for the spheroidal (blue lines), toroidal (yellow) and radial (black) components of the velocity field at $r = 0.95R_{\odot}$ for simulations (a) R1 to (d) R8. The dashed lines in panel (c) correspond to simulation R1x. The results of panels (c) and (d) indicate strongly anisotropic convection with divergent flows more energetic than the radial flows. The black and red dashed lines in panel (d) show the (Kolmogorov 1941, black dashed lines) and Rincon et al. (2017, red lines) predictions for the spectra of turbulent motions.

the anisotropy is larger, as can be seen in Fig. 6(c and d). In their spectrum for the horizontal velocity, the maximum is at $\ell \sim 5$ or 6, in fair agreement with our findings.

In the study performed by Featherstone & Hindman (2016a), including low- and high-resolution simulations, the situation is different. Their sets of simulations with density scale heights $N_{\rho} = 3$ and 4 are compatible with the experiments presented here. Unlike what is observed in Fig. 3(a), in their profiles of the RMS radial velocity component the maximum shifts towards the top boundary of the model with the increase of the resolution (also larger Rayleigh number). In their kinetic spectra, the largest scale $\ell = 1$, has the maximum power. In their low-resolution simulations, the power at low ℓ 's is larger and decreases for higher resolution, where the newly resolved motions acquire considerable energy. Thus, their inertial range becomes flat. This difference is intriguing. It might arise from the difference in the energy equation between this work and Featherstone & Hindman (2016a). However, both Featherstone & Hindman (2016a) and Hotta et al. (2019) consider somewhat similar energy equation, including a static background state and radiative diffusivity. On the other hand, Featherstone & Hindman (2016a) consider explicit viscous dissipation, whereas in this work and in Hotta et al. (2019) it comes from the numerical scheme.

3.2. Rotating solar convection

Here we present simulations that include the Coriolis force in the momentum equation, Eq. (2) (see Table 1). In numerical experiments not presented here, we noticed that the convergence to a steady state solution occurs faster if the initial conditions are random perturbations rather than the non-rotating relaxed state. Figure 7 depicts the morphological characteristics of the instantaneous radial flow in the orthographic projection at $r = 0.85R_{\odot}$ (see a,e and i panels for simulations R1x24, R2x24 and R4x24, respectively), and in the meridional plane (b,f,j); the latitudinal velocity in the meridional plane (c,g,k), and the longitudinal velocity (d,h,l).

The orthographic projection shows the elongated structures at equatorial latitudes also known as “banana cells”, characteristic of rotationally constrained motions taking the form of columns (Busse & Or 1986). For the cases R2x24 and R4x24 regions of strongly stretched structures are observed at intermediate latitudes. These are a consequence of the resulting large-scale shear. In the meridional plane, the convective motions at equatorial latitudes are not radial as in the non-rotating cases presented in Fig. 2, but elongated convective columns aligned with the rotation axis. At higher latitudes, there are multiple convective cells, exceeding the number in the non-rotating cases, with a certain tilt regarding the rotation axis. The latitudinal velocity (panels c, g and k) shows flow parcels that are aligned to the rotation axis. The number of these structures seem to increase with the resolution. Finally, the instantaneous snapshot of the longitudinal velocity evinces the sustained large-scale longitudinal flow resulting from each case. The low-resolution case shows an accelerated equator and deceleration towards high latitudes (panel d). The case R2x24 shows a fast rotating equator, a column of retrograde flow above the tangent cylinder, and a column of accelerated motions inside the tangent cylinder (h). In the case R4x24, the velocity at the equator diminishes, whereas the higher latitude acceleration increases and advances towards the poles (l). The sustainment of this longitudinal mean-flow, and its coupled meridional flow complement are discussed in §3.2.2.

Figure 8 compares the same averaged quantities presented in Fig. 3 between the rotating cases, R1x24, R2x24 and R4x24 (blue, red and green lines, respectively). For comparison, the results for the non-rotating models R1x and R4 are presented in black and gray dotted lines, respectively. It is expected that the amplitude of the velocity field components is quenched by the Coriolis force. This change is evident by comparing the continuous color lines with the dotted dark lines. For simulations R1x24 and R4x24 the mean radial velocity,

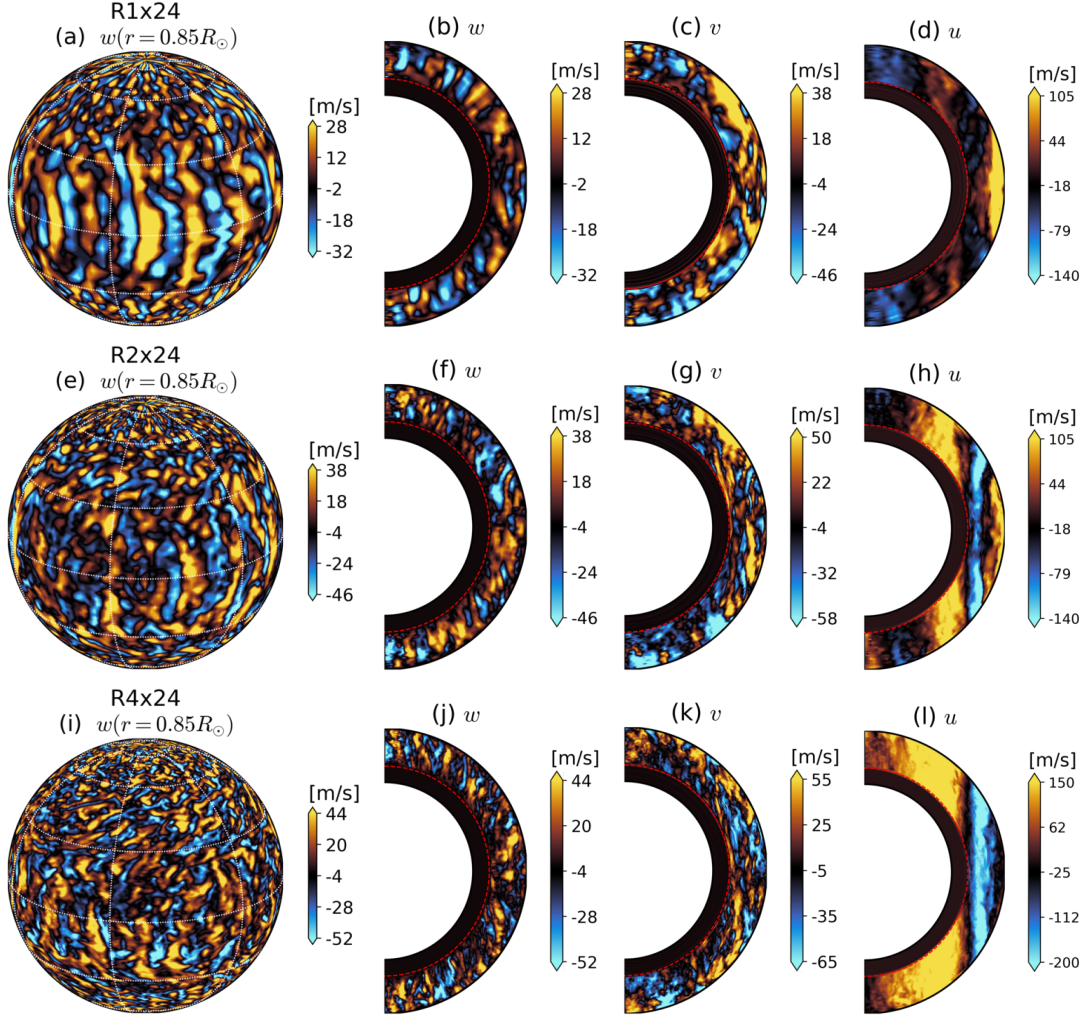


Figure 7. Same as Fig. 2 for simulations R1x24, R2x24 and R4x24, from top to bottom.

w_{rms} is $\sim 65\%$ and $\sim 70\%$ of the values for the cases R1x and R4, respectively (panel a). Most importantly for this paper is the observed trend of this quantity to acquire larger values with the increase of numerical resolution. Note also that the maximum of w_{rms} moves towards the upper boundary. The longitudinal component, u_{rms} (b), also decreases compared to the models without rotation, but the change is not as significant as for w_{rms} . It is noteworthy that the RMS horizontal motions slightly penetrate into the stable layer at $r \sim 0.7R_{\odot}$ (see vertical red line), and even at deeper layers there is a non-zero velocity. This non-vanishing velocity suggests that there is a weak level of turbulence in the stable layer. The perturbations of Θ (panel d) do not show significant changes in the convection zone with respect to the non-rotating cases. Also, there are no notable differences between simulations with different resolutions. However, at the bottom of the CZ, there is a

valley of negative perturbations that is deeper for higher resolution. A positive peak can be identified slightly below the CZ. Its location is roughly the same for all rotating cases. As seen below, these maxima appear as a consequence of the large-scale shear that establishes at the tachocline and their associated thermal wind balance.

The luminosity carried by the enthalpy flux resulting in the rotating simulations is presented in Fig. 9. It is interesting that, despite the differences in w_{rms} between simulations R1x24 to R4x24, the average of the correlations $w_{\text{rms}}\Theta'$ remain roughly the same for all cases, carrying roughly 25% of the solar luminosity. Also, despite that rotation makes w_{rms} to peak closer to the top of the domain, the maxima of L_e is shifted downwards, with respect to the non-rotating cases (see for comparison, the black dotted lines in the figure, corresponding to simulations R1x and R4). The figure also shows that

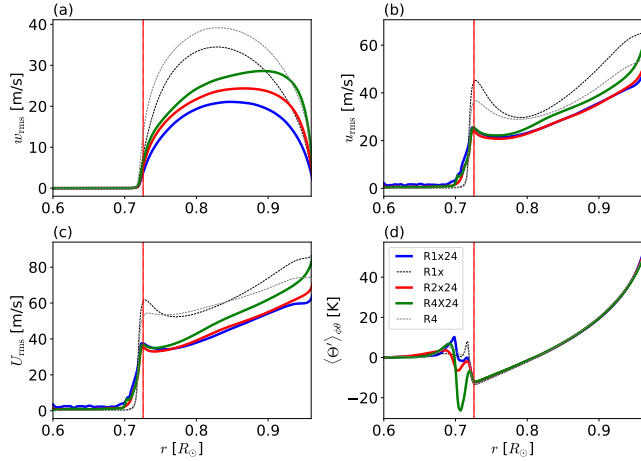


Figure 8. Same as Fig. 3 but for the rotating simulations with different resolutions, R1x24 (blue), R2x24 (red) and R4x24 (green). For comparison, the profiles corresponding to the non-rotating cases R1x and R4 are presented with black and gray dotted lines, respectively. The thin red vertical lines show the bottom of the convection zone.

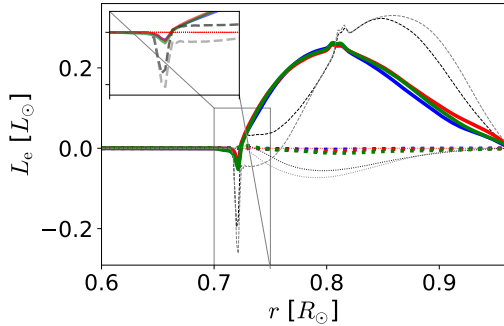


Figure 9. Luminosity carried by the enthalpy flux in the rotating simulations R1x24, R2x24 and R4x24. For comparison to the non-rotating cases, the dotted black and gray lines correspond to simulations R1x and R4, respectively. The inset focuses on the bottom of the convection zone and shows that overshooting decreases because of rotation. The dotted lines show the luminosity carried by the kinetic energy flux.

rotation diminishes overshooting. The bottom of the convection zone is focused in the inset in the figure. It clearly shows a considerable difference between the non-rotating cases, presented in dashed dark lines, and the rotating simulations. Finally, the dotted lines in the figures show the luminosity carried by the kinetic energy flux. It is evident that it is much smaller than in the non rotating cases. Therefore, the luminosity carried by convection, cf., the residual between L_e and L_k , is mostly due to the enthalpy flux.

3.2.1. Spectral analysis

The turbulent kinetic energy spectra of the rotating simulations at different depths (a-c) are presented in Fig. 10. In this figure only the decomposition in the \tilde{E}_Q (black line), \tilde{E}_S (blue) and \tilde{E}_T (yellow) components (Eq.12) is presented. The full kinetic spectra, (Eq. 11), follow the curves of the most energetic component, in this case, the toroidal kinetic energy. Note also that these spectra correspond to the turbulent velocity field, removing the axisymmetric component, $m = 0$ from the total velocity vector, i.e., $\mathbf{u}' = \mathbf{u} - \bar{\mathbf{u}}$. The thick dashed, dotted and solid lines correspond to the cases R1x24, R2x24 and R4x24, respectively. The spectra for the non-rotating case R4 is presented in thin continuous lines for comparison. For rotating convection they also reveal anisotropic motions. This time, however, the toroidal component is the dominant one. The radial velocity is the less energetic component. The anisotropy is more pronounced near the top of the model domain, with an energy difference of about two orders of magnitude at the scales of the most energetic motions. In the middle and bottom of the CZ, the anisotropy diminishes and the energy difference is about a factor of two.

As a consequence of the Coriolis force, the broad convective cells observed for non-rotating convection, with maximum energy at the harmonic degree $\ell \sim 3$, are broken into cells with scales peaking at $\ell \sim 30$ at the upper part of the domain and with most of the energy in \tilde{E}_T . At the middle and bottom there are peaks of energy at ℓ 's between 6 and 8.

It has been reported in both, HD (Featherstone & Hindman 2016b) and MHD simulations (Guerrero et al. 2019) that the spatial scale where the spectra peak depends on the Rossby number. The results presented in this study show that the Rossby number also changes with the numerical resolution. However, a shift in the spatial scale of the energy peak is observed only for the radial component at the domain's surface (panel a). \tilde{E}_Q peaks at $\ell \sim 30$ for simulation R1x24, $\ell \sim 40$ for simulation R2x24, and $\ell \sim 50$ for case R4x24. Concurrently, the energy increases by a factor of two to three between the low and the highest resolution cases. In the Sun, the radial spectral energy has a maximum at $\ell \sim 400$ for supergranular motions. Yet, as previously mentioned, supergranules are mainly divergent motions with most of the energy contained in the spheroidal energy component. Interestingly, a relevant change in the energy-containing scale of the horizontal velocity components with the mesh size is not observed. It is worth remembering here that the longitudinal velocity which largely contributes to \tilde{E}_T is the component used for measuring the observational spectra (Proxauf 2020). At large

ℓ 's the spectra decay with a scaling law faster than the Kolmogorov $\ell^{-5/3}$ rule at all depths (see the thin dotted lines). It is a remarkable result that the spectra do not show dramatic changes with resolution except the one described for \tilde{E}_r at surface levels. Surprisingly, the large-scale patterns deriving from these turbulent flows result in fully divergent outcomes, as will be presented below.

It is insightful to compare these findings with the results of the high resolution rotating simulation performed by Miesch et al. (2008). Their kinetic spectra show anisotropic motions at surface levels with the maxima energy in the horizontal velocity components and at the harmonic degrees $\ell = 20 - 30$. Their spectrum of the radial velocity component peaks at $\ell = 80$. Below the model top boundary their motions become more isotropic. These results are, in general, in good agreement with those presented in Fig. 10, i.e., with the increase of resolution the energy of the radial velocity shifts to larger energy and smaller scales. On the other hand, the spectra of the horizontal components seems to be independent on the resolution. Nonetheless, despite the agreement in the spectral properties, the resulting mean-flows of simulation R4x24 differ from their findings (see Fig. 6 of Miesch et al. 2008).

From the graphs presented in Fig. 10 stand out the maximums appearing between $6 \lesssim \ell \lesssim 10$. They are more evident at the middle and the bottom of the domain, Fig. 10(b and c). As a matter of fact, these peaks contain the largest energy at the bottom of the CZ. To identify to what motions these peaks correspond, Fig. 11 presents two-dimensional spectra for the simulation R1x24. These spectra are computed using Eq. (11) but not considering the sum over m and averaging only over time. The panels (b) and (c) reveal that the high energy harmonics in this particular range correspond to low-order longitudinal modes, $m = 1$ to 4. These are inertial modes, similar to Rossby waves, developing below the convection zone. It is observed that their maximal energy is at depth $r = 0.71R_\odot$ and, quite remarkably, these peaks appear at the same scales independently of the resolution. Because of their energy, which seems to propagate upwards to higher radial levels, these modes are likely dynamically important in the rotating convective system. Assessing the properties of these waves and their relevance is left for an independent study (Dias et al., in preparation).

The banana cells, clearly observed in Fig. 7(a, e, i) at $r = 0.85R_\odot$ have longitudinal wave numbers $16 < m < 20$, therefore in the (m, l) plane they are close to the diagonal in Fig. 11(b). At the top of the domain, the 2D spectrum shows large energies in the diagonal but also

below it. The analysis of solar motions by Getling & Kosovichev (2022) presents similar 2D spectra. At the deepest layers reached by their measurements, 19 Mm below the solar surface, their spectrum shows higher energy levels below the diagonal with scales peaking between $10 \lesssim \ell \lesssim 40$. The results presented in Fig. 11(a) resemble these observations.

3.2.2. Mean-flows and angular momentum transport

Turbulent inverse cascade effects allow the development of large-scale motions with spatial scales of the size of the system and temporal variations much longer than the convective turnover time. These motions can be separated into the longitudinal and meridional components namely, the differential rotation and meridional flow. The resulting differential rotation for simulation R1x24 is solar-like, accelerated (decelerated) at the equator (poles) with respect to the frame rotation rate Ω_0 , see panels Fig. 12(a,b). Yet, unlike the Sun where iso-rotation contours are conical, the profile has contours roughly cylindrical, aligned with the rotation axes.

The ambient state prevents the turbulent motions from penetrating into the stable layer below the thin overshooting region. Thus, a tachocline is formed at the transition between the radiative and convective zones. In the Sun, the tachocline is subjected to radiative spreading (Spiegel & Zahn 1992), and there is not yet a widespread agreement on the mechanisms that sustain its thickness. In most simulations including a sub-adiabatic layer below the convection zone, the tachocline spreads over time due to the imposed viscosity. In the ILES simulations presented here, there is no measurable viscous spreading of the tachocline in the stable layer during timescale of the simulations. This allows us to assess its role on the formation and sustain of large-scale flows.

The meridional circulation is represented in Fig. 12(c) through the mean latitudinal velocity in the meridional plane. In the northern hemisphere, the negative (positive) values of \bar{v} correspond to poleward (equatorward) motions. The graph shows several circulation cells appearing at latitudes between $\pm 35^\circ$ with amplitudes of a few m s^{-1} with the most prominent cells corresponding to clockwise circulation. At higher latitudes the meridional flow weakly reaches the poles at the upper layers and returns at deeper layers.

The DR of simulation R2x24, Fig. 12(d,e) still shows a fast equator. Nevertheless, a column of strong retrograde velocity appears outside the cylinder tangent to the model's tachocline. Physically, this is an expected outcome if the velocity of counterclockwise con-

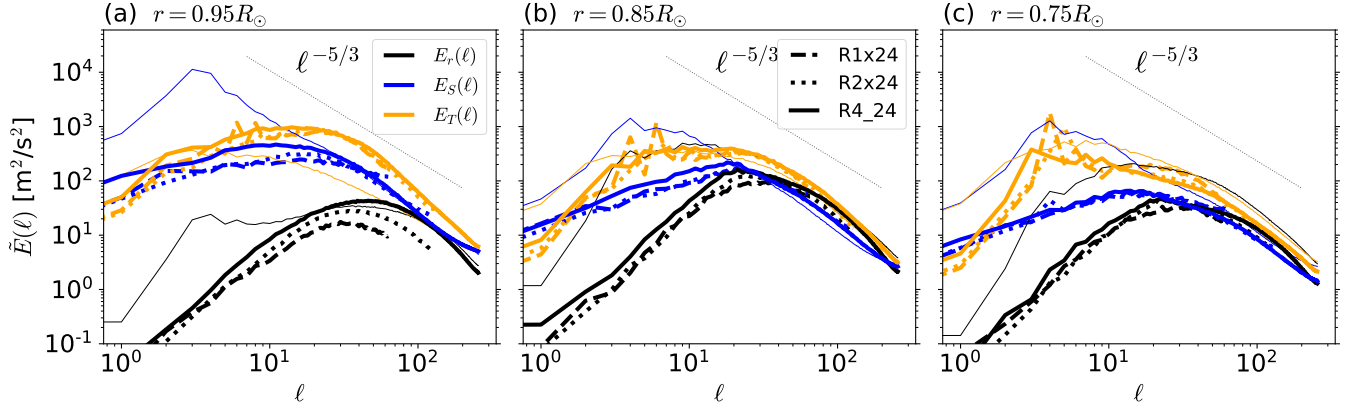


Figure 10. (a) to (c) Same as Fig. 6 for simulations R1x24 (dashed line), R2x24 (dotted) and R1_24 (solid). Note that the peak of the spectra of the rotating simulation is shifted towards the smaller scales, $\ell \sim 40$. Moreover, increasing resolution leads to larger power in the radial component, with maximum being shifted to the smaller scales. For comparison, the thin solid lines show the spectra of case R4 at the corresponding depths.

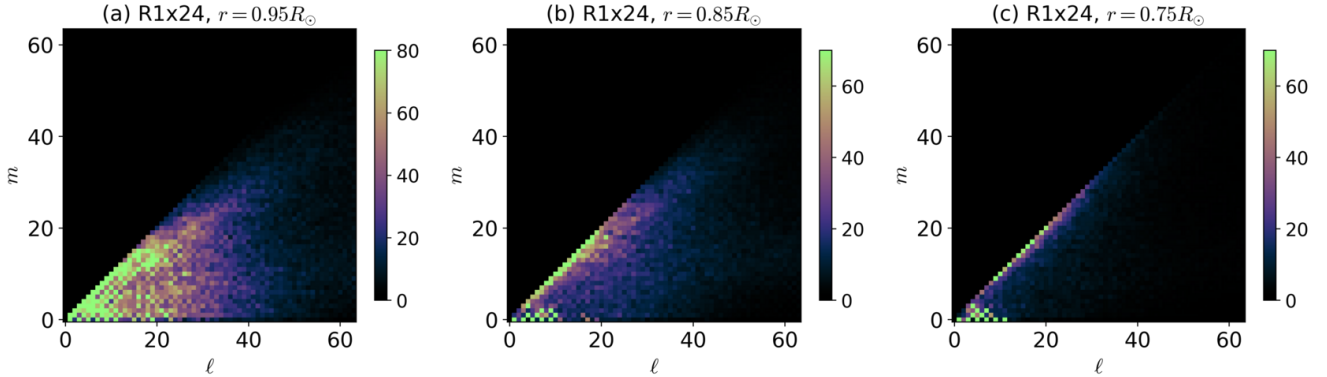


Figure 11. Two-dimensional kinetic energy spectra for the simulation R1x24 at the top, middle and bottom of the domain (a to c). The bottom left points observed in panels (b) and (c) correspond to inertial modes driven by the Coriolis force.

vective Busse columns is enhanced due to a large Rossby number (see e.g., Featherstone & Miesch 2015). Inside the tangent cylinder, there is a column of rotation with roughly the same speed as the equator, and slower poles at the highest latitudes. The same characteristics appear in simulation R4x24, however, increasing the resolution further decreases the equatorial speed and enhances the acceleration of the poles. The profiles of meridional flow remain similar in these simulations yet with stronger meridional flow velocities at intermediate to high latitudes. These enhanced meridional flows transport angular momentum towards the higher latitudes and explain the obtained polar acceleration.

Even though a solution independent of the grid resolution is not observed, and the highest resolution simulation is the farthest from the solar-like rotation, with the data at hand, it is possible to explore the redistribution of angular momentum as a function of the resolution to

get a better understanding of the processes that drive and sustain the mean-flow profiles.

The mean angular momentum, $\mathcal{L} = \varpi \rho_r \bar{u}$, where $\varpi = r \sin \theta$ is the lever arm and \bar{u} is the time and longitudinal average of u , evolves according to:

$$\frac{\partial \mathcal{L}}{\partial t} = -\nabla \cdot (\varpi [\rho_r (\bar{u} + \varpi \Omega_0) \bar{\mathbf{u}}_m + \rho_r \overline{u' \mathbf{u}'_m}]), \quad (13)$$

where, $\bar{\mathbf{u}}_m$, and \mathbf{u}'_m are the mean and turbulent meridional (r and θ) components of the velocity field, respectively. More explicitly, the terms inside the divergence are the fluxes of angular momentum,

$$\begin{aligned} \mathcal{F}_r^{\text{RS}} &= \rho_r \varpi \overline{u' w'}, \\ \mathcal{F}_\theta^{\text{RS}} &= \rho_r \varpi \overline{u' v'}, \\ \mathcal{F}_r^{\text{MC}} &= \rho_r \varpi (\bar{u} + \varpi \Omega_0) \bar{w}, \\ \mathcal{F}_\theta^{\text{MC}} &= \rho_r \varpi (\bar{u} + \varpi \Omega_0) \bar{v}, \end{aligned} \quad (14)$$

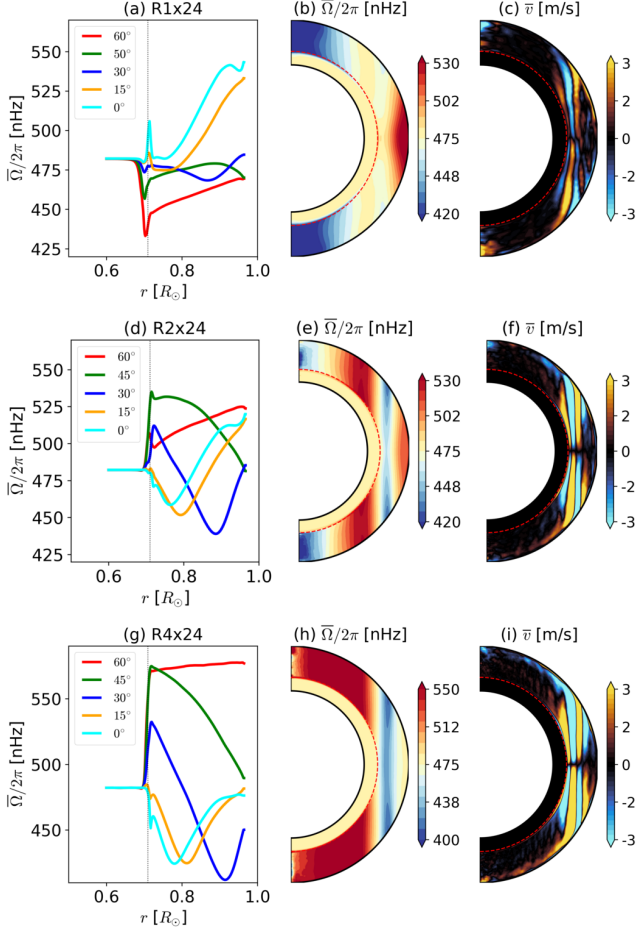


Figure 12. Left and middle panels: differential rotation as a function of radius for different latitudes, and in the meridional plane, respectively, for simulations R1x24, R2x24, and R4x24, from top to bottom. Right panels: mean profile of the latitudinal velocity in the meridional plane. In the northern hemisphere negative (positive) values correspond to poleward (equatorward) flows.

which arise from the small-scale correlations of the turbulent flow, cf. Reynolds stresses (RS) and from the mean profiles of DR and MC that establish at a statistically steady state. It is expected that during this stage, the LHS of the equation vanishes; therefore, the four fluxes of Eq. 14 should balance with each other. The net radial and latitudinal angular momentum transport may be estimated by computing the fluxes across spherical and conical surfaces, respectively (see Brun & Toomre 2002) as

$$\begin{aligned}
 I_r(r) &= \int_0^\pi \mathcal{F}_r(r, \theta) r^2 \sin \theta d\theta \\
 I_\theta(\theta) &= \int_{r_b}^{r_t} \mathcal{F}_\theta(r, \theta) r \sin \theta dr,
 \end{aligned} \tag{15}$$

where:

$$\begin{aligned}
 \mathcal{F}_r &= \mathcal{F}_r^{\text{MC}} + \mathcal{F}_r^{\text{RS}} \\
 \mathcal{F}_\theta &= \mathcal{F}_\theta^{\text{MC}} + \mathcal{F}_\theta^{\text{RS}}.
 \end{aligned} \tag{16}$$

Since r runs from bottom to top, positive (negative) values of I_r correspond to upward (downward) angular momentum flux. Similarly, θ runs from the north to the south poles; thus, positive (negative) I_θ corresponds to equatorward (poleward) flux in the northern hemisphere. The fluxes of angular momentum for the simulations R1x24, R2x24 and R4x24, integrated in radius and latitude, are presented in the top and bottom rows of Fig. 13, panels (a) to (c), respectively. For evaluation of the independent contributions of the RS and the MC, the integrals for $\mathcal{F}_r^{\text{MC}}$ and $\mathcal{F}_\theta^{\text{MC}}$ (red lines), and $\mathcal{F}_r^{\text{RS}}$ and $\mathcal{F}_\theta^{\text{RS}}$ (blue lines) are presented separately. The black dashed lines show the sum of the MC and RS contributions.

For the lowest resolution case, panel (a), the RS transports angular momentum downwards at the bottom half of the convection zone and upwards at the upper half. Increasing the resolution leads to an increase in the radial flux (panels b and c). However, for the cases R2x24 and R4x24, the RS flux is negative, inward, in most of the convection zone, with boundary regions of positive, upward, flux at the bottom and top of the domain. The radial RS flux is well balanced by the MC flux, and the sum of the two fluxes is roughly consistent with zero.

The amplitude of the latitudinal fluxes also increases with the numerical resolution. In all the cases the RS flux pumps angular momentum towards the equator. Unlike the radial flux, the MC flux does not balance its turbulent counterpart and even shows a different profile for each case. In simulation R1x24, I_θ^{MC} has the same sign as I_θ^{RS} at lower and intermediate latitudes. Therefore, the net transport of angular momentum is equatorward. This explains the solar-like profile observed in Fig. 12(a, b). The black dashed line in the bottom panel of Fig. 13(a) clearly shows that the two fluxes do not balance each other. In these hydrodynamic simulations the only term missing in Eq. (13) is the viscous flux. While in the Sun this term must be irrelevant, in the low-resolution case, it appears in the form of effective viscosity. This numerical contribution results in an angular momentum flux with values compatible with the RS and MC fluxes.

In simulations R2x24 and R4x24, the balance between RS and MC fluxes is better, as evidenced by the smaller values reached by the black dashed line relative to the values of I_θ^{RS} and I_θ^{MC} . Yet, the balance is not perfect (bottom row of panels b and c). The MC flux assumes the opposite sign of RS and advects angular momen-

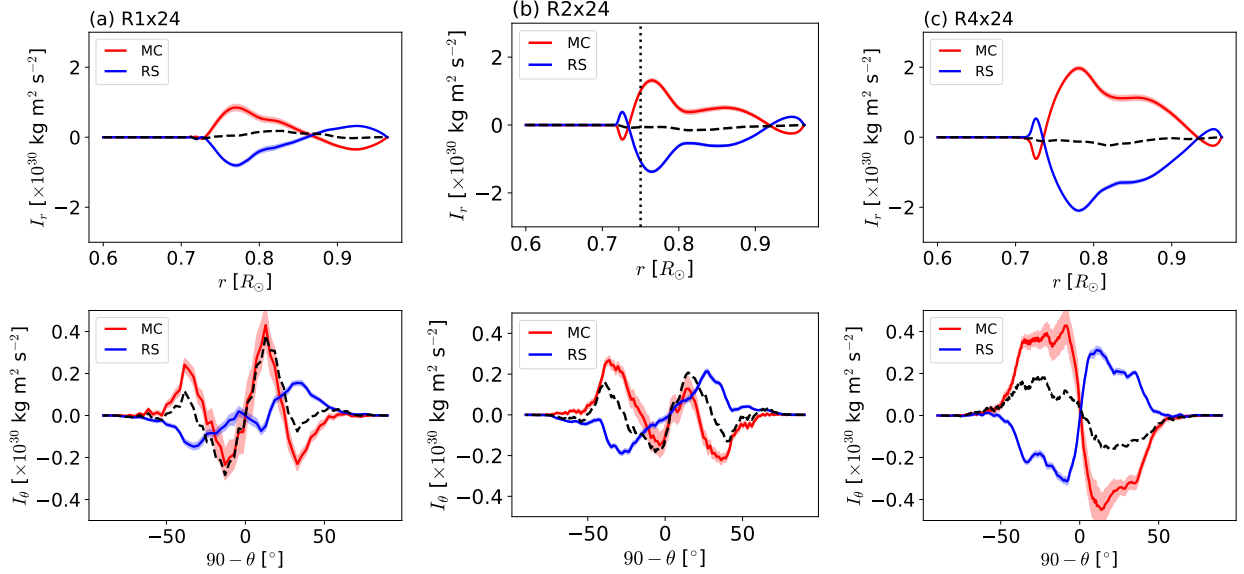


Figure 13. Angular momentum fluxes integrated over spherical surfaces at different r (upper panels) and conical surfaces at latitudes $90 - \theta$ (bottom), for the simulations (a) R1x24, (b) R2x24 and (c) R4x24. The red and blue lines correspond to the MS and RS contributions, the dashed black line is the sum of both contributions.

tum towards the poles. Notice that in the three cases the resolution increases only in the horizontal direction. The results of Nogueira et al. (2022) with the EULAG-MHD code in 2D Cartesian simulations indicate that the effective viscosity scales as $N^{-2.7}$, with N being the horizontal resolution. Thus, changing N_ϕ and N_θ by a factor of two and four results in a change in the effective viscosity with a factor of ~ 7 and ~ 300 , respectively. Although in the spherical coordinates the scaling of the effective viscosity with the resolution may be different, it is not unrealistic to expect changes by a factor larger than 10. It is good to have in mind, however, that this viscosity is non-linear and non-homogeneous, being larger in regions where the flow has steeper variations. The bottom row of Fig. 13(c) demonstrates the weaker influence of the effective viscosity on the angular momentum dynamics. In this case I_θ^{MC} has almost twice the amplitude of I_θ^{RS} . Therefore, the sum of the two has also half of the amplitude of I_θ^{MC} and its contribution aims to settle the balance. The profiles of I_θ^{MC} explain the transition of the DR from the accelerated equator to accelerated poles. It is worth mentioning here that the profiles in Fig. 13(c) are compatible with those of Miesch et al. (2008), with the exception of an enhanced MC latitudinal flux in case R4x24. Nevertheless, unlike the differential rotation profile observed in Fig. 12(g, h), they obtain a solar-like rotation. There are several differences between the two modeling approaches. The more relevant ones are perhaps the different values of the Prandtl number (0.25 in their case and ~ 1 in this

work) and the initial condition of the simulation as well as the total evolution time. They enforce a solar-like profile and then evolve the simulation for ~ 3 years, whereas the models presented here start from random thermal fluctuations and evolve the system for 20 years.

The large-scale flows observed in Fig. 12 are sustained by the fluctuations around average values of the angular momentum fluxes. The shadow involving the profiles presented in Fig. 13 depict the standard error, $\sigma_e = \sigma/\sqrt{n}$, where σ is the variance and n the number of samples in the average. It is clear from the figure that the MC flux has larger deviations from the mean profile and that these deviations increase for higher resolutions. This result is not surprising given the smaller viscous friction that the flow experiences in the higher resolution cases. The fluctuations are sustained by turbulent convection in turn driven by the buoyancy force. Therefore, Eq. (13) does not entirely describes the sustainability of the mean-flows.

Before providing an overview on the sustainment of the DR and MC, it is illustrative to compute the divergence of the fluxes on the RHS of Eq. (13). Including the minus sign in front, the results are the axial torques;

$$\mathcal{T}^{RS} = -\frac{1}{r^2} \frac{\partial(r^2 F_r^{RS})}{\partial r} - \frac{1}{r \sin \theta} \frac{\partial(F_\theta^{RS} \sin \theta)}{\partial \theta}, \quad (17)$$

$$\mathcal{T}^{MC} = -\frac{1}{r^2} \frac{\partial(r^2 F_r^{MC})}{\partial r} - \frac{1}{r \sin \theta} \frac{\partial(F_\theta^{MC} \sin \theta)}{\partial \theta}, \quad (18)$$

due to the RS and the MC, respectively. These quantities are presented in Fig. 14. On average, in the steady-

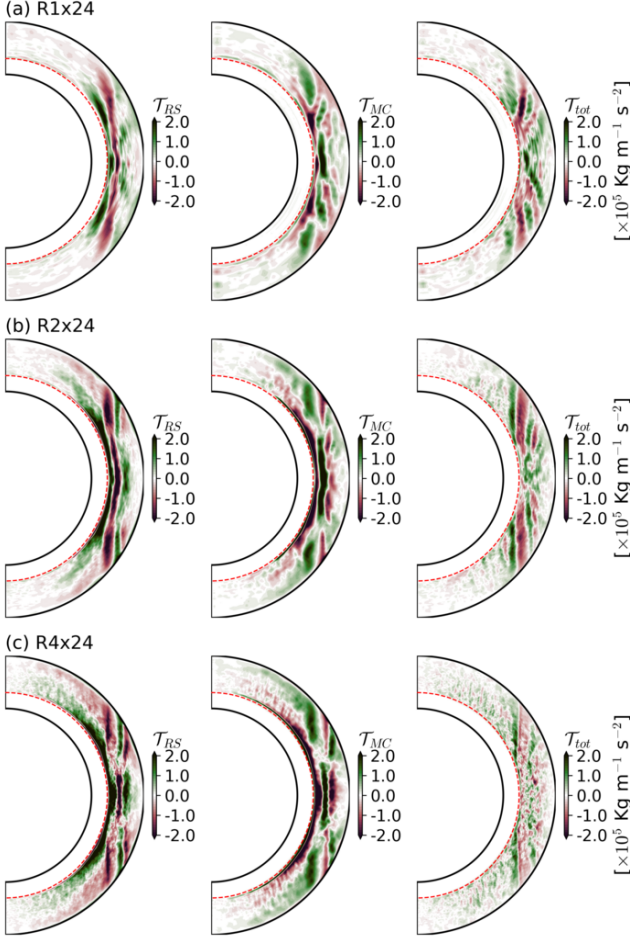


Figure 14. Axial torques due to the RS (left column), the MC (middle), and the sum of the RS and MC (right) torques presented in the meridional plane for the simulations R1x24 (top row), R2x24 (middle) and R4x24 (bottom).

state, the RS produce a torque that changes sign with radius and latitude. The profiles from simulations R1x24 to R4x24 are similar, although, for the higher resolution cases, the torque becomes stronger, better aligned with the axis outside the tangent cylinder, and seems to reach higher latitudes. For balancing these torques, the meridional motions form closed loops whose circulation has axial torques in the opposite direction to the RS. This process is called gyroscopic pumping. It is sustained from deviations of the thermal wind balance as will be seen in the following section. The direction of the meridional flows may be identified by writing Eq. (13), with $\partial\mathcal{L}/\partial t = 0$, as,

$$\rho_r \bar{\mathbf{u}}_m \cdot \nabla (\varpi^2 \Omega) = -\nabla \cdot (\rho_r \varpi \overline{\mathbf{u}'_m u'}) = -\mathcal{T}^{RS}, \quad (19)$$

and with the known profiles of Ω and \mathcal{T}^{RS} (Figs. 12 and 14). As a simple example, let's consider the simulation R4x24, with constant θ at the equator, equation (19)

becomes

$$\rho_r \bar{w}_{eq}(r) \frac{\partial}{\partial r} (r^2 \Omega_{eq}(r)) = -\frac{1}{r^2} \frac{\partial}{\partial r} (r^2 F_{r,eq}^{RS}(r)). \quad (20)$$

The radial derivative at the LHS is positive for all r , whereas the radial derivative at the RHS is negative for $0.72R_\odot \lesssim r \lesssim 0.77$, positive for $0.77R_\odot \lesssim r \lesssim 0.82$ and negative again for $0.82R_\odot \lesssim r \lesssim 0.9$, from where it is positive, see the leftmost panel of Fig. 14(c). Thus, because of the minus sign in the RHS, the profile of $\bar{w}_{eq}(r)$ has to have the opposite sign to $\frac{\partial}{\partial r} (r^2 F_{r,eq}^{RS}(r))$. We have numerically verified that this relation is obeyed for all values of r .

In general, Fig. 14 shows that the MC torque roughly has the same profile than the RS torque yet with the opposite sign. The third column of the figure depicts $\mathcal{T}_{tot} = \mathcal{T}^{RS} + \mathcal{T}^{MC}$. It shows that the balance is not perfect, suggesting the contribution of axial torques by the effective viscosity. With the increase of the resolution, panels (a) to (c), the values of the axial torques become higher, the balance seems to improve, and \mathcal{T}_{tot} is evidently less coherent. Both changes are a consequence of the diminished viscous resistance to the turbulent motions.

3.2.3. Differential temperature and thermal-wind balance

Both quantities on the LHS of Eq. (19) are sustained from the departures of the equilibrium state through fluctuations driven by convection, which in turn is sustained by the buoyancy force. An equation including this contribution may be obtained by computing the vorticity by taking the curl of Eq. (2). The longitudinal component of the vorticity contains various terms that sustain the meridional balance (see e.g., Miesch & Hindman 2011; Passos et al. 2017, for derivation and discussion). The inertial, \mathcal{I} , and the baroclinic, \mathcal{B} , terms are the most relevant (Kitchatinov 2013) leading to the thermal wind balance (TWB) equation,

$$\mathcal{I} = \varpi \frac{\partial \Omega^2}{\partial z} = \mathcal{B} + \mathcal{D} = \frac{g}{\Theta_r} \frac{\partial \Theta'}{\partial \theta} + \mathcal{D}, \quad (21)$$

where z is the vertical axis in cylindrical coordinates, such that $\partial_z = \cos \theta \partial_r - r^{-1} \sin \theta \partial_\theta$, and \mathcal{D} incorporates all other forces in the meridional plane, including the contribution of the diagonal as well as the meridional components of the Reynolds stress tensor.

Departures from the TWB due to fluctuations of the LHS term induce meridional motions via the gyroscopic pumping seen from Eq. (19). Similarly, latitudinal differential temperatures result in meridional flows driven by baroclinicity. Equations (19) and (21) are obviously coupled. As mentioned above, meridional motions

are necessary to balance the angular momentum, these motions are generated by deviations from the TWB. Fig. 15 shows the temperature fluctuations as a function of latitude. From the figure, it is possible to determine whether the gyroscopic pumping or the baroclinic force drives the meridional flow. For better visualization of the latitudinal differential temperature, two different scales are considered at the left and right of the panels (a) to (c), corresponding to simulations R1x24 to R4x24, respectively. The scale at the left (right) Y -axis shows T' at the top (bottom) of the convective layer. Comparing the blue and red curves indicates that the latitudinal contrast is small (less than one degree) at the top of the domain, yet it reaches tens of Kelvins at the bottom of the CZ. Furthermore, whereas at the top of the domain the equator is colder than the poles for all cases, below the CZ the equator is colder only for simulation R1x24, and large temperature contrast between a warmer equator and colder poles is found for simulation R4x24. The shadows show the deviation from the mean.

Given the profiles of Fig. 15, baroclinicity should result in motions with prominent clockwise circulation for the case R1x24, and prominent counterclockwise circulation for cases R2x24 and R4x24. This is clearly not observed in the rightmost panels of Fig. 12, except perhaps at intermediate to higher latitudes in case R4x24. The main source of the meridional motions observed outside the tangent cylinder is likely the departure from thermal wind balance about the inertia term, \mathcal{I} , which corresponds to the gyroscopic pumping.

The contribution of the meridional forces to the generation of meridional circulation can be better understood through the comparison of the two most important terms of the meridional force balance equation, namely the inertial, \mathcal{I} , and the baroclinic, \mathcal{B} , terms. If the two terms cancel to each other, the system is in TWB. Whenever the balance is violated, either transiently or after temporal and longitudinal averages, vorticity in the meridional plane, i.e., meridional circulation, is induced. Fig. 16 shows contours of \mathcal{I} (first column), and \mathcal{B} (second column) in the meridional plane. The third column shows the departure of TWB via the residual $\mathcal{B} - \mathcal{I}$.

The first thing to notice in Fig. 16 is the qualitative and quantitative similarity of the meridional profiles \mathcal{I} and \mathcal{B} . However, the third column shows that the balance is not perfect. Note that the scale of the residual is half of the inertial and baroclinic terms. Thus, the deviation from TWB is smaller yet considerable. As expected, this deviation is more prominent outside the tangent cylinder, where the meridional circulation cells are observed. Not surprisingly, it increases with the numerical resolution providing enhanced meridional circulation

(note that the opposite happens with the axial torques, Fig. 14, i.e., the residual decreases with the increase of resolution).

The departures from the TWB by meridional drivers such as the meridional Reynolds stress component sustain a meridional flow which is stronger at higher resolution because the numerical viscosity offers less and less resistance to these motions. The meridional motions compensate for the angular momentum transported by the Reynolds stresses. In the low resolution case, where viscosity is high, the angular momentum balance due to MC is insufficient and the positive (negative) values of I_{θ}^{RS} in the northern (southern) hemisphere efficiently accelerate the equator. In the high-resolution case, the MC motions develop with less friction and better compensate for the angular momentum fluxes (see I_{θ}^{MC} in Fig 13). As a matter of fact, they are sufficiently strong to accelerate the poles. In the Sun, the molecular viscous resistance is insignificant. Thus, there is always the magnetic field, which may provide the large or small-scale Maxwell stresses necessary to allow an effective equatorial transport of angular momentum resulting in solar-like rotation. Yet it is not the only possibility to solve this issue.

In mean-field models of differential rotation (see Kitchatinov 2013, for a review), the TWB is almost exact in the bulk of the convection zone. And departures are obtained at the boundary layers in such a way that a strong poleward meridional flow develops at the near-surface shear layer, and the equatorial return flow occurs at tachocline levels. The theory for the formation of the NSSL developed by Miesch & Hindman (2011) is in agreement with this view, suggesting that, in this layer, the inertia term is balanced by turbulent stresses rather than by the baroclinic force. It is worth remarking that in the simulations presented here the NSSL is not considered, and these boundary effects may be a relevant missing element. Nonetheless, baroclinicity is not sufficient to balance the inertial meridional force as presented above. It is possible that the turbulent motions developed in most of the current global simulations are not a reliable representation of the high Re, low Pr turbulence occurring inside the Sun.

Another remarkable point from Fig. 16 is that the tachocline does not seem to act as a boundary layer generating strong departures of the TWB as suggested in mean-field models. It has usually been assumed that latitudinal gradients of temperature may be responsible for the deviation from the cylindrical towards the conical iso-rotation contours observed in the Sun. This seems to work in global simulations that do not include the tachocline where a latitudinal differential tempera-

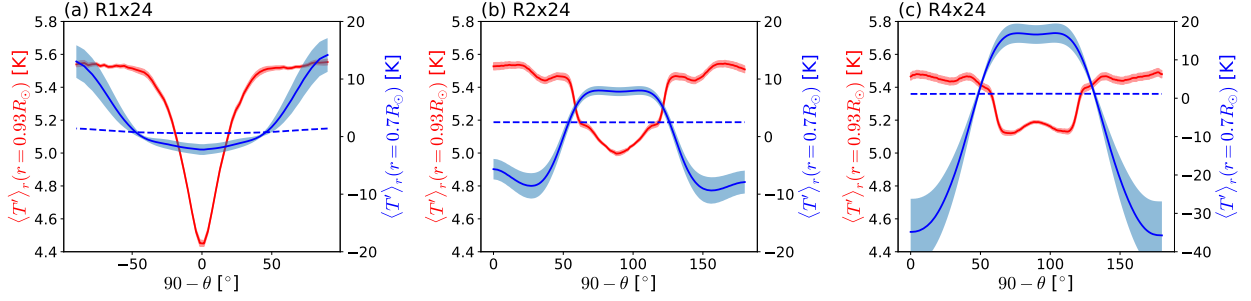


Figure 15. Latitudinal variations of temperature perturbations: the red and blue lines correspond to profiles of temperature perturbations at the surface and the bottom of the convection zone for the models (a) R1x24, (b) R2x24, and (c) R4x24. The contrast at the two radial levels is different; therefore two different scales at the left and right Y axis are considered. The dashed line shows a third radial level at $r = 0.66$, where perturbations are not expected. The $\langle \rangle_r$ indicates radial average centered in $r = 0.71R_\odot$ and $r = 0.93R_\odot$ in a radial layer of thickness $0.04R_\odot$.

ture is imposed as a boundary condition (Miesch et al. 2006). The simulations presented in this work, including the tachocline, demonstrate otherwise. Consider, for instance, the low-resolution simulation, R1x24. The slower north pole and fast equator make the variation of $\bar{\Omega}$ along the direction of the rotation axes (z) most negative at the poles, than at $\sim 40^\circ$, where the convection zone rotates at the same speed than the stable layer. This is compensated by a negative gradient of Θ' , and consequently in T' . Conversely, in case R4x24, $\bar{\Omega}$ goes from a slower stable layer towards a faster north pole, generating a positive signal for the term \mathcal{I} . This is compensated by a positive temperature gradient of ~ 40 K which is also evident in \mathcal{B} . Therefore, it is possible to conclude that, in our simulations, the differential temperature is a reaction of the baroclinic force to the gradient of the angular velocity the z direction. Once the balance is established, the outcome are roughly cylindrical iso-rotation contours independently of the rotation being faster at the equator or at the poles.

4. CONCLUSIONS

We have performed HD convection simulations with the EULAG-MHD code in a spherical shell whose thermodynamic stratification resembles the upper part of the solar radiation layer and the convection zone up to $r = 0.96R_\odot$. We have considered cases without and with rotation. The thermal driving, considered here through an ambient state, results in an enthalpy flux corresponding to $\sim 0.3L_\odot$ for the non-rotating cases and $\sim 0.2L_\odot$ for the rotating simulations. Keeping fixed all the parameters in the governing equations, we explore how progressively increasing the numerical resolution affects the simulation results. We solve the equations in their inviscid form, therefore, the only dissipation of momentum and heat is delegated to the truncation terms of the numerical method. Arguably, in this form we can

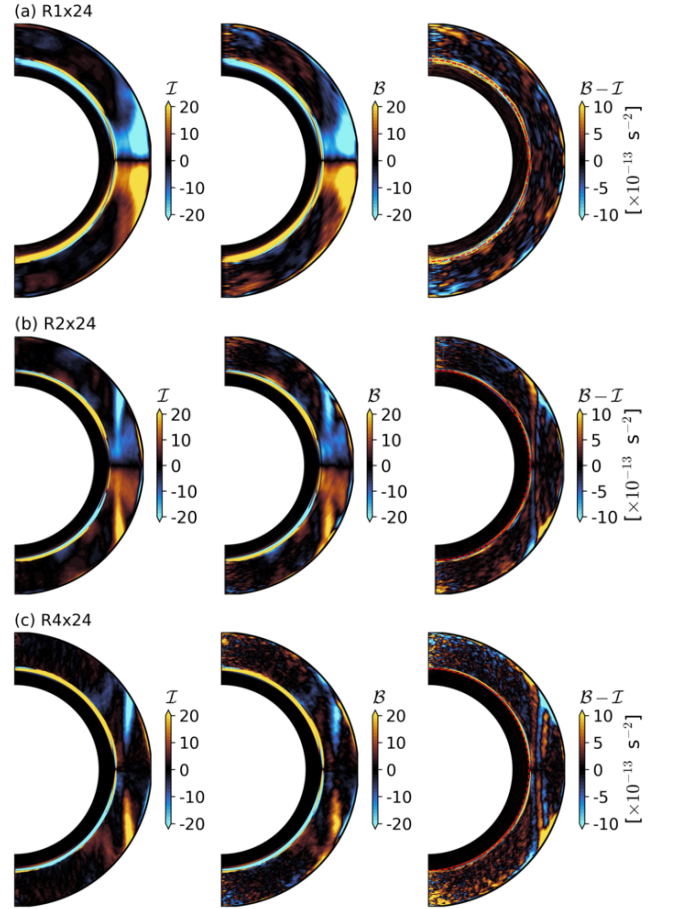


Figure 16. Inertia, \mathcal{I} (left), and baroclinic, \mathcal{B} (middle) terms of the TWB, Eq. 21. The right column shows the residual $\mathcal{B} - \mathcal{I}$.

achieve larger values of the effective Reynolds number with less computational resources. It is expected that at sufficiently high Re , the contribution of viscosity to the transport of linear and angular momentum should be

negligible and the dynamics of the system is defined by the properties of the turbulent motions. Our main goals are to identify the properties of the fluid as a function of the resolution and evaluate the challenges of achieving grid independent results for this complicated problem.

For the non-rotating cases our findings can be summarized as follows:

- The low-order velocity moments and turbulent spectra of the non-rotating simulations do not show significant changes between the highest resolution cases R4 and R8, indicating that the ILES convergence might be achieved at a resolution not much higher than R8.
- The ambient state considered in the model captures the sharp transition in the Brunt-Väisälä frequency. High resolution in the radial direction is needed for this stiffness to be captured by the velocity field, especially its horizontal components. The gradient of U_{rms} between stable and unstable layers increases with N_r but seems to saturate at $N_r = 256$ grid points (this value corresponds to a radial grid size, $dz = 982$ km). This resolution also appears sufficient to capture the 4.5 density scale heights considered in the model (3.7 only in the convection zone).
- The convective motions resulting from cases R4 and R8 are characterized by anisotropic convection with most of the energy in the divergent component of the horizontal flow at the top of the domain. Because of the thickness of the convection zone, the power spectra peaks at larger scales, 1000-1400 Mm ($\ell \sim 3-4$), in good agreement with similar simulations performed at a much higher resolution (Hotta et al. 2014, 2019). There is also agreement with some characteristics of supergranulation obtained by Rincon et al. (2017). These motions, of course, have maximum energy at much smaller scales presumably because are driven by thermal perturbations injected in a thin boundary layer.
- In case R1x, we increased the resolution of the simulation in the r direction and kept N_ϕ and N_θ equal to case R1. Despite the lack of detailed small-scale structures, the flow properties of this case correlate well with those obtained for cases R4 and R8. For this reason, we consider this resolution our starting point for the rotating simulations.

More important for the solar dynamics is the case of rotating convection. We performed three simulations

where the radial grid size is kept constant, and only the horizontal resolution is increased. These cases appear in Table 1 as R1x24, R2x24 and R4x24. The rotation period of these simulations is 24 days. It is slightly shorter than the solar period, yet it results in solar-like differential rotation in the lower resolution experiment, R1x24. The main results of these simulations are summarized below:

- The perturbations of Θ , and more importantly, the luminosity carried by the enthalpy flux, are roughly the same for all simulations. Nevertheless, the amplitude of the velocity components increases with the resolution. This is more evident in the RMS profile of the radial component, w_{rms} . The difference seems to be larger between R4x24 and R2x24, than between R2x24 and R1x24. This suggests that for simulations accounting for the rotation, grid independent solutions are hard to achieve.
- The turbulent kinetic spectra shows strongly anisotropic motions near the top of the convection zone. The anisotropy decreases at the middle and bottom of the convection zone. As expected, rotation imprints vorticity in the flow. Thus, the energy of the toroidal part of the horizontal flows becomes dominant. Interestingly, the scale with maximal energy in the horizontal motions appears independent of the grid size. On the other hand, the energy in the radial component increases with the resolution, and the peak of the spectrum shifts towards larger harmonic degrees, i.e, the smaller scales become more energetic. This seems to be a robust result when comparing our findings with those of the high resolution simulation of Miesch et al. (2008).
- The change in the resulting mean-flows as a function of grid resolution is dramatic. The output values of the Rossby number go from ~ 0.56 to ~ 0.65 , and in this range, we observe a transition from solar-like to anti-solar differential rotation. The meridional circulation shows multiple cells aligned to the cylinder tangent to the tachocline. The meridional speed increases with the resolution, as it does the high latitudinal poleward flow.
- The physics behind the differential rotation transition is understood through the integrated angular momentum balance and thermal wind balance (TWB). It may be summarized as follows. At low resolution, the total viscosity is high; this offers strong resistance to the meridional motions

driven by transient departures of the TWB. In this case, the angular momentum balance in the latitudinal direction is dominated by the viscosity and the Reynolds stresses which pump angular momentum towards the equator. With the increase of the resolution, the effective viscosity might decrease sharply, consistent with the 2D results of (Nogueira et al. 2022). Thus, there is a better angular momentum balance between the Reynolds stresses and the meridional circulation, arguably the most relevant processes to account for in HD simulations. This angular momentum equilibrium favors polar acceleration because there is a steady departure in the meridional force balance and strong poleward meridional flows carry angular momentum with small friction.

- In the simulations presented here, the latitudinal variations of temperature at the base of the convection zone are a consequence of TWB and not a results of departure from TWB as commonly assumed (see the concluding paragraph in § 3.2.3). Thus, although there are strong temperature gradients between the equator and pole, the contours of iso-rotation are roughly cylindrical.

The results presented here correspond to an enthalpy flux carrying only one-fourth of the solar luminosity, and the rotation period is compatible to the sidereal rotation period of the Sun. Extrapolating the observed trend to solar values would result in a larger discrepancy with the solar differential rotation. Also, the energy contained in scales corresponding to $\ell \sim 30 - 40$ would be higher than what it is found in recent solar observations (Proxauf 2020), suggesting that increasing the resolution does not lead to a solution of the convective conundrum. These problems, of course, are not specific to the EULAG-MHD simulations but are present in most global convection models. The results of the recent simulations of Hotta & Kusano (2021) suggest that the small-scale dynamo might be a solution. This field may act as friction that quenches the velocity and contributes to the angular momentum balance, leading to solar-like rotation. Other MHD simulations indicate that the large-scale magnetic field may contribute in the same direction (Fan & Fang 2014; Karak et al. 2015; Guerrero et al. 2016). To this date, there are no simulations where both, small- and large-scale contributions of the magnetic field, the usual suspect, are considered.

Nonetheless, the entire problem may reside in the fact that the convection driven in the global simulations is

not an accurate representation of the turbulent motions in the solar interior. The reason for this could be the enormous differences in the parameter regime between the Sun and the simulations. It has also been suggested that the deep solar convection may depend on the physics occurring in the uppermost 50Mm (or less) of the Sun (Spruit 1997), which are barely considered in global simulations. In this boundary layer, the effective cooling provided by hydrogen ionization destabilizes the plasma generating cold downward plumes. Thus, the turbulent motions in the deep solar convection zone may be driven by this penetrative entropy rain (Brandenburg 2016). In this sense, deep solar convection can be seen as a non-local process in a buoyantly neutral layer. The numerical experiments performed by Cossette & Rast (2016) demonstrated this concept in a Cartesian box. Their results show that the dominant convective scales depend on the thickness of the boundary layer. Concurrently, the fast convective motions in this layer are not constrained by the solar rotation and produce a negative shear which, in turn, accelerates meridional motions producing the observed surface latitudinal velocity (Miesch & Hindman 2011). Recent simulations of Kitiashvili et al. (2022) showed that turbulent convection in the upper part of the NSSL can generate the radial differential rotation and meridional circulation. However, it is still uncertain how the turbulent correlations generated by non-local convection can sustain the solar differential rotation below the NSSL. Thus, it is worth exploring this possibility and its consequences for the mean-flows in global simulations. The pursuit of numerical convergence is also worth more computational efforts. A database of simulations with varying resolutions is necessary for studying the changes in the turbulence properties at different Rayleigh and Reynolds numbers. It can also be used for the experimentation of sub-grid scale methods that allow realistic simulations at a lower computational cost. These goals will be pursued in future works.

We thank Bonnie Zaire for her comments on the manuscript. This work was partly funded by NASA grants NNX14AB70G, 80NSSC20K0602, and 80NSSC20K1320. NCAR is sponsored by the National Science Foundation. The simulations were performed in the NASA supercomputer Pleiades

REFERENCES

- Böhm-Vitense, E. 1958, *ZA*, 46, 108
- Brandenburg, A. 2016, *ApJ*, 832, 6,
doi: [10.3847/0004-637X/832/1/6](https://doi.org/10.3847/0004-637X/832/1/6)
- Brown, B. P., Browning, M. K., Brun, A. S., Miesch, M. S., & Toomre, J. 2008, *ApJ*, 689, 1354, doi: [10.1086/592397](https://doi.org/10.1086/592397)
- Brun, A. S., & Toomre, J. 2002, *ApJ*, 570, 865,
doi: [10.1086/339228](https://doi.org/10.1086/339228)
- Busse, F. H., & Or, A. C. 1986, *Journal of Fluid Mechanics*, 166, 173, doi: [10.1017/S0022112086000095](https://doi.org/10.1017/S0022112086000095)
- Chen, R., & Zhao, J. 2017, *ApJ*, 849, 144,
doi: [10.3847/1538-4357/aa8eec](https://doi.org/10.3847/1538-4357/aa8eec)
- Christensen-Dalsgaard, J., Dappen, W., Ajukov, S. V., et al. 1996, *Science*, 272, 1286,
doi: [10.1126/science.272.5266.1286](https://doi.org/10.1126/science.272.5266.1286)
- Cossette, J.-F., Charbonneau, P., Smolarkiewicz, P. K., & Rast, M. P. 2017, *The Astrophysical Journal*, 841, 65
- Cossette, J.-F., & Rast, M. P. 2016, *ApJL*, 829, L17,
doi: [10.3847/2041-8205/829/1/L17](https://doi.org/10.3847/2041-8205/829/1/L17)
- Fan, Y., Abbett, W. P., & Fisher, G. H. 2003, *ApJ*, 582, 1206, doi: [10.1086/344798](https://doi.org/10.1086/344798)
- Fan, Y., & Fang, F. 2014, *ApJ*, 789, 35,
doi: [10.1088/0004-637X/789/1/35](https://doi.org/10.1088/0004-637X/789/1/35)
- Featherstone, N. A., & Hindman, B. W. 2016a, *ApJ*, 818, 32, doi: [10.3847/0004-637X/818/1/32](https://doi.org/10.3847/0004-637X/818/1/32)
- . 2016b, *ApJL*, 830, L15,
doi: [10.3847/2041-8205/830/1/L15](https://doi.org/10.3847/2041-8205/830/1/L15)
- Featherstone, N. A., & Miesch, M. S. 2015, *ApJ*, 804, 67,
doi: [10.1088/0004-637X/804/1/67](https://doi.org/10.1088/0004-637X/804/1/67)
- Gastine, T., Yadav, R. K., Morin, J., Reiners, A., & Wicht, J. 2014, *MNRAS*, 438, L76, doi: [10.1093/mnras/slt162](https://doi.org/10.1093/mnras/slt162)
- Getling, A. V., & Kosovichev, A. G. 2022, arXiv e-prints, arXiv:2201.00638. <https://arxiv.org/abs/2201.00638>
- Ghizaru, M., Charbonneau, P., & Smolarkiewicz, P. K. 2010, *ApJL*, 715, L133,
doi: [10.1088/2041-8205/715/2/L133](https://doi.org/10.1088/2041-8205/715/2/L133)
- Gizon, L., & Birch, A. C. 2012, *Proceedings of the National Academy of Science*, 109, 11896,
doi: [10.1073/pnas.1208875109](https://doi.org/10.1073/pnas.1208875109)
- Gizon, L., Cameron, R. H., Pourabadian, M., et al. 2020, *Science*, 368, 1469, doi: [10.1126/science.aaz7119](https://doi.org/10.1126/science.aaz7119)
- Greer, B. J., Hindman, B. W., Featherstone, N. A., & Toomre, J. 2015, *ApJL*, 803, L17,
doi: [10.1088/2041-8205/803/2/L17](https://doi.org/10.1088/2041-8205/803/2/L17)
- Grinstein, F., Margolin, L., & Rider, W. 2007, *Implicit Large Eddy Simulation: Computing Turbulent Fluid Dynamics* (Cambridge University Press)
- Guerrero, G., Smolarkiewicz, P. K., de Gouveia Dal Pino, E. M., Kosovichev, A. G., & Mansour, N. N. 2016, *ApJL*, 828, L3, doi: [10.3847/2041-8205/828/1/L3](https://doi.org/10.3847/2041-8205/828/1/L3)
- Guerrero, G., Smolarkiewicz, P. K., Kosovichev, A. G., & Mansour, N. N. 2013, *ApJ*, 779, 176,
doi: [10.1088/0004-637X/779/2/176](https://doi.org/10.1088/0004-637X/779/2/176)
- Guerrero, G., Zaire, B., Smolarkiewicz, P., et al. 2019, *The Astrophysical Journal*, 880, 6
- Hanasoge, S. M., Duvall, T. L., & Sreenivasan, K. R. 2012, *Proceedings of the National Academy of Science*, 109, 11928, doi: [10.1073/pnas.1206570109](https://doi.org/10.1073/pnas.1206570109)
- Hathaway, D. H., & Upton, L. 2014, *Journal of Geophysical Research (Space Physics)*, 119, 3316,
doi: [10.1002/2013JA019432](https://doi.org/10.1002/2013JA019432)
- Hathaway, D. H., & Upton, L. A. 2021, *ApJ*, 908, 160,
doi: [10.3847/1538-4357/abcbfa](https://doi.org/10.3847/1538-4357/abcbfa)
- Hotta, H. 2018, *ApJL*, 860, L24,
doi: [10.3847/2041-8213/aacafb](https://doi.org/10.3847/2041-8213/aacafb)
- Hotta, H., Iijima, H., & Kusano, K. 2019, *Science Advances*, 5, 2307, doi: [10.1126/sciadv.aau2307](https://doi.org/10.1126/sciadv.aau2307)
- Hotta, H., & Kusano, K. 2021, *Nature Astronomy*, 5, 1100,
doi: [10.1038/s41550-021-01459-0](https://doi.org/10.1038/s41550-021-01459-0)
- Hotta, H., Rempel, M., & Yokoyama, T. 2014, *ApJ*, 786, 24, doi: [10.1088/0004-637X/786/1/24](https://doi.org/10.1088/0004-637X/786/1/24)
- . 2015, *ApJ*, 798, 51, doi: [10.1088/0004-637X/798/1/51](https://doi.org/10.1088/0004-637X/798/1/51)
- Käpylä, P. J., Käpylä, M. J., & Brandenburg, A. 2014, *A&A*, 570, A43, doi: [10.1051/0004-6361/201423412](https://doi.org/10.1051/0004-6361/201423412)
- Käpylä, P. J., Mantere, M. J., Guerrero, G., Brandenburg, A., & Chatterjee, P. 2011, *A&A*, 531, A162,
doi: [10.1051/0004-6361/201015884](https://doi.org/10.1051/0004-6361/201015884)
- Karak, B. B., Käpylä, P. J., Käpylä, M. J., et al. 2015, *A&A*, 576, A26, doi: [10.1051/0004-6361/201424521](https://doi.org/10.1051/0004-6361/201424521)
- Kippenhahn, R., Weigert, A., & Weiss, A. 2013, *Stellar Structure and Evolution*, doi: [10.1007/978-3-642-30304-3](https://doi.org/10.1007/978-3-642-30304-3)
- Kitchatinov, L. L. 2013, in *Solar and Astrophysical Dynamos and Magnetic Activity*, ed. A. G. Kosovichev, E. de Gouveia Dal Pino, & Y. Yan, Vol. 294, 399–410,
doi: [10.1017/S1743921313002834](https://doi.org/10.1017/S1743921313002834)
- Kitiashvili, I. N., Kosovichev, A. G., Mansour, N. N., & Wray, A. A. 2015, *ApJ*, 809, 84,
doi: [10.1088/0004-637X/809/1/84](https://doi.org/10.1088/0004-637X/809/1/84)
- Kitiashvili, I. N., Kosovichev, A. G., Wray, A. A., Sadykov, V. M., & Guerrero, G. 2022, arXiv e-prints, arXiv:2203.01484. <https://arxiv.org/abs/2203.01484>
- Kolmogorov, A. 1941, *Akademiia Nauk SSSR Doklady*, 30, 301
- Lipps, F. B., & Hemler, R. S. 1982, *Journal of the Atmospheric Sciences*, 39, 2192,
doi: [10.1175/1520-0469\(1982\)039<2192:ASAODM>2.0.CO;2](https://doi.org/10.1175/1520-0469(1982)039<2192:ASAODM>2.0.CO;2)
- Miesch, M. S., Brun, A. S., DeRosa, M. L., & Toomre, J. 2008, *ApJ*, 673, 557, doi: [10.1086/523838](https://doi.org/10.1086/523838)

- Miesch, M. S., Brun, A. S., & Toomre, J. 2006, *ApJ*, 641, 618, doi: [10.1086/499621](https://doi.org/10.1086/499621)
- Miesch, M. S., & Hindman, B. W. 2011, *ApJ*, 743, 79, doi: [10.1088/0004-637X/743/1/79](https://doi.org/10.1088/0004-637X/743/1/79)
- Nogueira, H. D., Guerrero, G., Smolarkiewicz, P. K., & Kosovichev, A. G. 2022, *ApJ*, 928, 148, doi: [10.3847/1538-4357/ac54b7](https://doi.org/10.3847/1538-4357/ac54b7)
- Ossendrijver, M. 2003, *A&A Rv*, 11, 287, doi: [10.1007/s00159-003-0019-3](https://doi.org/10.1007/s00159-003-0019-3)
- Passos, D., Miesch, M., Guerrero, G., & Charbonneau, P. 2017, *A&A*, 607, A120, doi: [10.1051/0004-6361/201730568](https://doi.org/10.1051/0004-6361/201730568)
- Proxauf, B. 2020, PhD thesis, Georg August University of Göttingen, Germany
- Prusa, J. M., Smolarkiewicz, P. K., & Wyszogrodzki, A. A. 2008, *Computers & Fluids*, 37, 1193
- Rincon, F., & Rieutord, M. 2018, *Living Reviews in Solar Physics*, 15, 6, doi: [10.1007/s41116-018-0013-5](https://doi.org/10.1007/s41116-018-0013-5)
- Rincon, F., Roudier, T., Schekochihin, A. A., & Rieutord, M. 2017, *A&A*, 599, A69, doi: [10.1051/0004-6361/201629747](https://doi.org/10.1051/0004-6361/201629747)
- Rogachevskii, I., Kleeorin, N., Kitiashvili, I. N., et al. 2011, arXiv e-prints, arXiv:1102.1206. <https://arxiv.org/abs/1102.1206>
- Schaeffer, N. 2013, *Geochemistry, Geophysics, Geosystems*, 14, 751, doi: [10.1002/ggge.20071](https://doi.org/10.1002/ggge.20071)
- Scherrer, P. H., Schou, J., Bush, R. I., et al. 2012, *Sol. Phys.*, 275, 207, doi: [10.1007/s11207-011-9834-2](https://doi.org/10.1007/s11207-011-9834-2)
- Schou, J., Antia, H. M., & Basu, S. e. a. 1998, *ApJ*, 505, 390, doi: [10.1086/306146](https://doi.org/10.1086/306146)
- Smolarkiewicz, P. K. 2006, *International Journal for Numerical Methods in Fluids*, 50, 1123
- Smolarkiewicz, P. K., & Charbonneau, P. 2013, *J. Comput. Phys.*, 236, 608, doi: [10.1016/j.jcp.2012.11.008](https://doi.org/10.1016/j.jcp.2012.11.008)
- Spiegel, E. A., & Zahn, J. P. 1992, *A&A*, 265, 106
- Spruit, H. C. 1997, *Mem. Soc. Astron. Italiana*, 68, 397. <https://arxiv.org/abs/astro-ph/9605020>
- Stejko, A. M., Kosovichev, A. G., & Pipin, V. V. 2021, *ApJ*, 911, 90, doi: [10.3847/1538-4357/abec70](https://doi.org/10.3847/1538-4357/abec70)
- Strugarek, A., Beaudoin, P., Charbonneau, P., Brun, A. S., & do Nascimento, J.-D. 2017, *Science*, 357, 185, doi: [10.1126/science.aal3999](https://doi.org/10.1126/science.aal3999)
- Ulrich, R. K. 2010, *ApJ*, 725, 658, doi: [10.1088/0004-637X/725/1/658](https://doi.org/10.1088/0004-637X/725/1/658)
- Wray, A. A., Bensassi, K., Kitiashvili, I. N., Mansour, N. N., & Kosovichev, A. G. 2015, arXiv e-prints, arXiv:1507.07999. <https://arxiv.org/abs/1507.07999>